Cell Reports
Article

Autophagy Impairment in Muscle Induces Neuromuscular Junction Degeneration and Precocious Aging

Silvia Carnio,[1] Francesca LoVerso,[1] Martin Andres Baraibar,[9] Emanuela Longa,[5] Muzamil Majid Khan,[7] Manuela Maffei,[5] Markus Reischl,[7] Monica Canepari,[5] Stefan Loefler,[12] Helmut Kern,[12] Bert Blaauw,[2] Bertrand Friguet,[9] Roberto Bottinelli,[5,6] Rüdiger Rudolf,[7,8,10,11] and Marco Sandri[1,2,3,4,13,*]

[1]Dulbecco Telethon Institute, Venetian Institute of Molecular Medicine, 35129 Padova, Italy
[2]Department of Biomedical Sciences, University of Padova, 35121 Padova, Italy
[3]Institute of Neuroscience, Consiglio Nazionale delle Ricerche, 35121 Padova, Italy
[4]Department of Medicine, McGill University, Montreal QC H3A 0G4, Canada
[5]Department of Molecular Medicine and Interuniversity Institute of Myology, University of Pavia, Via Forlanini 6, 27100 Pavia, Italy
[6]Fondazione Salvatore Maugeri (IRCCS), Scientific Institute of Pavia, 27100 Pavia, Italy
[7]Institut für Angewandte Informatik, Karlsruhe Institute of Technology, 76128 Karlsruhe, Germany
[8]Institut für Toxikologie und Genetik, Karlsruhe Institute of Technology, 76128 Karlsruhe, Germany
[9]Laboratoire de Biologie Cellulaire du Vieillissement, UR4, Université Pierre et Marie Curie-Paris 6, 75252 Paris Cedex 05, France
[10]Institut für Molekular und Zellbiologie, University of Applied Sciences Mannheim, 68163 Mannheim, Germany
[11]Institut für Medizintechnologie, University of Applied Sciences Mannheim and University of Heidelberg, 68163 Mannheim, Germany
[12]Ludwig Boltzmann Institute of Electrical Stimulation and Physical Rehabilitation, 1171 Vienna, Austria
[13]Telethon Institute of Genetics and Medicine (TIGEM), 80131 Napoli, Italy
*Correspondence: marco.sandri@unipd.it

http://dx.doi.org/10.1016/j.celrep.2014.07.061

SUMMARY

The cellular basis of age-related tissue deterioration remains largely obscure. The ability to activate compensatory mechanisms in response to environmental stress is an important factor for survival and maintenance of cellular functions. Autophagy is activated both under short and prolonged stress and is required to clear the cell of dysfunctional organelles and altered proteins. We report that specific autophagy inhibition in muscle has a major impact on neuromuscular synaptic function and, consequently, on muscle strength, ultimately affecting the lifespan of animals. Inhibition of autophagy also exacerbates aging phenotypes in muscle, such as mitochondrial dysfunction, oxidative stress, and profound weakness. Mitochondrial dysfunction and oxidative stress directly affect acto-myosin interaction and force generation but show a limited effect on stability of neuromuscular synapses. These results demonstrate that age-related deterioration of synaptic structure and function is exacerbated by defective autophagy.

INTRODUCTION

Aging is accompanied by numerous tissue phenotypes. Changes that occur in postmitotic organs are considered hallmarks of aging. A common feature of aged organisms is functional alteration and gradual loss of muscle mass and force. A deficit of muscle innervation due to motor-neuron loss is believed to have a major contribution to age-dependent muscle wasting, also called sarcopenia. This age-acquired deficit in muscles contributes profoundly to reduced quality of life in elderly people and predisposes them to an increased risk of morbidity, disability, and mortality (Visser and Schaap, 2011). The etiology of sarcopenia is multifaceted and involves several intrinsic and extrinsic factors. Despite the clinical, social, and economic relevance of sarcopenia, the precise mechanisms for the age-related loss of muscle mass and function are not yet fully understood. Age-related changes in muscle are complex, with key features including myofiber atrophy, profound weakness that is partially independent of muscle mass loss, myofiber degeneration, accumulation of dysfunctional mitochondria, and increased oxidative stress. Until recently, it was thought that age-associated atrophy and weakness were secondary to motor-neuron loss in the brain or in the spinal cord. However, this hypothesis has been recently challenged. In fact, little neuronal death occurs in most areas of the aging nervous system, and there is no decline of lower motor neurons during aging (Chai et al., 2011; Morrison and Hof, 1997). Conversely, it is emerging that neuromuscular junctions (NMJs) and their interactions with myofibers are greatly altered during aging, resulting in a loss of muscle innervation (Chai et al., 2011; Valdez et al., 2010). Oxidative stress and decreased release of trophic factors are independent influences on NMJ integrity and contribute to denervation (Jang et al., 2010, 2012; Jang and Van Remmen, 2011). However, to date, it is not known whether myofiber denervation is due to deleterious changes in muscle cells themselves, in neurons, or both.

Two lifestyle adaptations, caloric restriction and exercise (Jang et al., 2012; Valdez et al., 2010), have been consistently demonstrated to extend lifespan and, in parallel, to mitigate

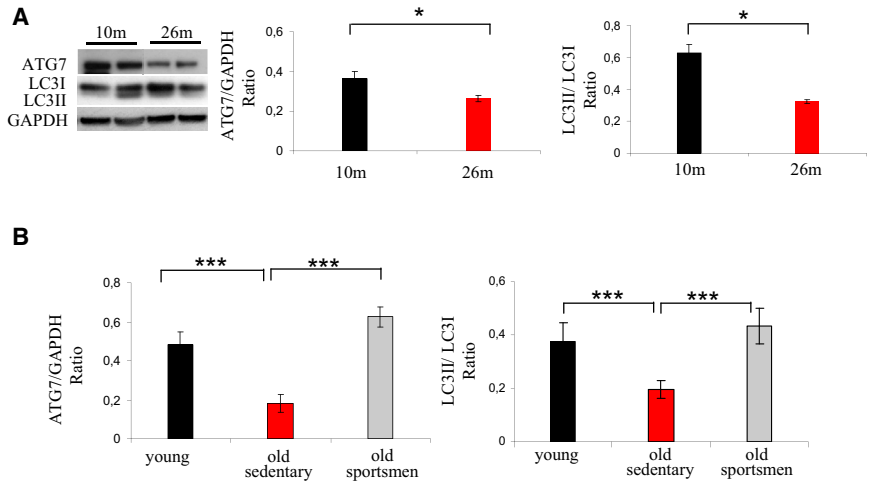

Figure 1. Autophagy Is Impaired during Aging

(A) Representative immunoblotting for the critical E1-like enzyme, ATG7, LC3II, and LC3I on muscle extracts from gastrocnemius of 10- and 26-month-old mice. The graphs show the quantification of ATG7 protein and the LC3II/LC3I ratio. Values are mean ± SEM; n = 4 of each condition; *p < 0.05.

(B) Aging reduces whereas exercise maintains expression of ATG7 and LC3 lipidation in humans. The graphs show the quantification of ATG7 protein and LC3II/LC3I ratio revealed by immunoblotting on muscle biopsies. Values are mean ± SEM; n = 6 young; n = 10 elderly, sedentary men; and n = 4 senior sportsmen; ***p < 0.0001.

age-related alterations of NMJ. Macroautophagy, hereafter named autophagy, is activated by both of these conditions in skeletal muscles and other tissues (Grumati et al., 2010, 2011a, 2011b; He et al., 2012; Rubinsztein et al., 2011; Wohlgemuth et al., 2010). Autophagy is a highly conserved homeostatic mechanism used for the degradation and recycling of bulk cytoplasm, long-lived proteins, and organelles through the lysosomal machinery (Mizushima and Komatsu, 2011). The autophagy machinery generates double membrane vesicles (autophagosomes) that engulf and sequester target cellular components (Mizushima and Komatsu, 2011). Autophagosomes are then delivered to and fuse with lysosomes to degrade their contents. Therefore, autophagy can be defined as a process of cytosolic renovation. In mammals, the relationship between autophagy inhibition and aging is still largely phenomenological and correlative. Conversely, robust genetic evidence in worms and flies clearly demonstrates this relationship. Deficient expression of ATG1, ATG7, ATG8, BECN1 (Beclin1), and SESTRIN1 (which is also required for basic autophagy) shortens the lifespan of the fruit fly *D. melanogaster* and of the nematode *C. elegans* (Lee et al., 2010b; Rubinsztein et al., 2011; Simonsen et al., 2008). On the other hand, increased autophagy contributes to longevity, and mutation of essential Atg genes prevents the gain of longevity (Meléndez et al., 2003). A recent report shows that aging can be controlled by a single tissue; overexpression of FOXO transcription factor or its target EIF4EBP1 in fly skeletal muscle abolishes the age-associated decline in autophagy and increases longevity (Demontis and Perrimon, 2010). We previously identified FOXO3A as a regulator of autophagy (Mammucari et al., 2007, 2008; Zhao et al., 2007), and genetic variations in the human FOXO3A have been linked to longevity in multiple population studies (Kenyon, 2010). The role of autophagy in sarcopenia in mammals is still controversial. Both impaired and excessive autophagy have been associated with aging sarcopenia (Wenz et al., 2009; Wohlgemuth et al., 2010). However, loss-of-function experiments that support the involvement of autophagy in aging sarcopenia are still lacking. Here, we show that specific inhibition of autophagy in skeletal muscle leads to abnormalities in motor neuron synapses that ultimately lead to denervation whereas accumulation of dysfunctional mitochondria triggers oxidation of contractile elements, causing a decrease in force generation.

RESULTS

Autophagy Declines during Aging

Age-related muscle loss is believed to result from a general decline of protein synthesis or an enhancement of protein breakdown. To study autophagy in aging, we monitored the expression of autophagy markers, such as LC3 (MAP1LC3A) and the critical E1-like enzyme, ATG7, in mice and humans. Aged mice showed a decline of ATG7 protein and, concurrently, of LC3 lipidation when compared to young animals (Figure 1A). Then we tested whether this decrease of the autophagy system occurs in humans. An important decrease of ATG7 protein and LC3II was found in muscle biopsies of elderly sedentary (sarcopenic) subjects (Figure 1B). Because exercise activates autophagy and counteracts most age-related characteristics, including the decline of muscle mass (Zampieri et al., 2014), we tested whether long-life regular exercise in humans was able to prevent the reduction of these autophagy markers. ATG7 protein and LC3II were maintained in muscle biopsies of senior sportsmen that had been previously shown to have better muscle mass and strength than elderly sedentary subjects (Zampieri et al., 2014).

Autophagy Inhibition Affects Neuromuscular Synaptic Morphology and Function

To mimic the decrease of ATG7 in aging, we characterized muscle-specific autophagy-deficient ($Atg7^{-/-}$) mice that we have generated (Masiero et al., 2009). The absence of autophagy caused a significant reduction of animal survival (Figure 2A). Morphological analyses of aged mice showed higher levels of atrophy, center-nucleated fibers, and inflammation in $Atg7^{-/-}$ muscles compared to age-matched controls (Figures 2B and S1A). Fiber size was affected in $Atg7^{-/-}$, and fibers displayed great variability in dimension. Some fibers atrophied to a level that made them hardly detectable (Figure 2C). These small fibers did not express the typical markers of regeneration

and, therefore, are adult atrophic myofibers (data not shown). Quantification of the cross-sectional area (CSA) of Atg7$^{-/-}$ revealed that, although muscle atrophy was present in both oxidative and glycolytic fibers, it was more pronounced in the latter (Figures 2D and 2E).

The deterioration of *Atg7*$^{-/-}$ muscles was also confirmed by the increase of center-nucleated fibers (Figure 2H). Correspondingly, *Atg7*$^{-/-}$ muscles were weaker than controls both in adult and elderly mice (Figures 2F and 2G). Given that the features of atrophic fibers resemble denervated fibers, and a decline in innervation and loss of motor units are known to be important endogenous causes of sarcopenia, we tested whether denervation plays a role in the phenotype of *Atg7*$^{-/-}$ mice. We first examined the expression pattern of the neural cell adhesion molecule (NCAM), a molecule that is enriched in the postsynaptic membrane of the NMJ but largely absent in adult myofibers. However, NCAM is re-expressed along the entire muscle fiber after the loss of innervation. Immunohistochemistry revealed that, during aging, there is a progressive increase of NCAM-positive fibers in controls. Importantly, *Atg7*$^{-/-}$ muscles showed 5- to 7-fold more NCAM-positive fibers when compared to age-matched controls both in adult and elderly mice (Figures 2I–2K and S1B). The expression of two other markers of denervation, MuSK (MUSK) and the acetylcholine receptor (AChR) γ-subunit (CHRNG) were significantly more upregulated in *Atg7*$^{-/-}$ muscles (Figure 2L). To confirm these findings, we used a recently described in vivo imaging approach where two distinct AChR pools are differently color labeled (Röder et al., 2008, 2010) to monitor NMJ morphology and stability.

Automated image analysis revealed that, in contrast to control muscles, NMJs of adult *Atg7* knockout mice showed fragmented morphology (Figures 3A and 3B) and instability (Figures 3A and 3B). Whereas in controls, the changes in morphology and instability progressively increased with age, this was not the case in *Atg7* knockout mice (Figure 3B). NMJs of both adult and aged *Atg7*-deficient animals showed significantly more fragmentation and AChR turnover than 26-month-old (aged) control animals (Figure 3B, right panel).

Exocytic and endocytic processes mediate delivery of newly formed AChR and retrieval of old AChR, respectively. We monitored the localization and the number of the vesicles containing AChR. Inhibition of autophagy led to accumulation of vesicles close to the endplates that contain bungarotoxin (BGT) (Figures 3C and 3D), further corroborating an impairment of AChR turnover and of endosome trafficking. To determine whether alteration in endosome trafficking might also affect MuSK, a kinase that affects a plethora of signaling pathways that are important for NMJ stability, we monitored MuSK localization. Immunohistochemistry revealed that most MuSK colocalized with AChR at the plasma membrane in control fibers (Figure 3E). Importantly, *Atg7*$^{-/-}$ caused a significant loss of MuSK on the plasma membrane and a concomitant enrichment of internalized MuSK (Figure 3E). These findings confirm an alteration of AChR and MuSK recycling and localization in *Atg7*$^{-/-}$ mice. To determine whether the changes of NMJ are secondary to p62 (p62/SQSTM) accumulation into aggregates that clear signaling factors such as NRF2 or secondary to inhibition of the conjugation system, we knocked down p62 in *Atg7*$^{-/-}$. For in vivo transfection experiments, we used bicistronic vectors that simultaneously encode small hairpin RNAs (shRNAs) and GFP. In this way, detection of GFP fluorescence allowed us to monitor the efficiency of transfection and the changes that occurred to p62-positive aggregates. After 14 days of transfection, *Atg7*$^{-/-}$ tibialis anterior (TA) muscle was cleared by p62-positive inclusions (Figure S2A). However, despite the absence of p62-positive aggregates, the percentage of denervated NCAM-positive fibers was not improved (Figure S2B).

To understand the role of autophagy in age-related NMJ alterations, we used the inducible muscle-specific *Atg7* knockout mice that we have recently generated (Masiero et al., 2009). The *Atg7* gene was acutely deleted in 22-month-old mice, and mice were sacrificed 3 months later. Western blots for p62 and LC3 revealed that autophagy was successfully blocked in aged mice (Figure 4A). The inhibition of autophagy in old mice led to an exacerbation of muscle mass degeneration as revealed by the increase of centronucleated fibers and the decrease of CSA (Figures 4B and 4C). Fiber size distribution analysis revealed that acute *Atg7* deletion led to an enrichment of small fibers when compared to controls (Figure S3), suggesting that denervation occurred in a discrete number of fibers. We then monitored NMJ to determine whether autophagy inhibition in old mice was sufficient to destabilize muscle-nerve interaction. *Atg7* deletion led to a significant increase of denervated NCAM-positive fibers (Figure 4D). Denervation is also supported by the finding that the *MuSK* transcript is significantly induced in *Atg7*$^{-/-}$ (Figure 4E). Acute inhibition of autophagy in aged mice caused a significant loss of MuSK on the myofiber plasma membrane and a concomitant enrichment of internalized MuSK protein (Figure 4F).

Rescue of Atg7 Expression in Aged Mice Improves Neuromuscular Synaptic Function

To determine the involvement of autophagy in NMJ maintenance during aging, we overexpressed ATG7 protein in 26-month-old *Atg7*$^{f/f}$ mice to restore normal autophagy flux in aged mice. ATG7 expression was sufficient to increase LC3-positive vesicles in sarcopenic muscles (Figure 5A). When we monitored the effect of ATG7 expression on NMJ of aged mice, we found a significant improvement in morphology; NMJ was significantly less fragmented than age-matched controls (Figures 5B and 5C). Correspondingly, restoring autophagy in aged mice led to a decrease of vesicles close to the endplates that contain BGT, further corroborating a reactivation of AChR turnover and of endosome trafficking (Figure 5D). This was confirmed by the fact that MuSK localization was improved by the expression of ATG7 (Figure 5E). Rescuing ATG7 protein and autophagy led to a reduction of denervated NCAM-positive fibers that returned to the values of adult mice (Figure 5F). Finally, improvement of autophagy flux and NMJ morphology resulted in an enhancement in muscle mass (Figure 5G).

Autophagy Inhibition Enhances Mitochondrial Dysfunction and Oxidative Stress that Induces NMJ Instability

One potential explanation of age-related loss of muscle mass and innervation is due to accumulation of dysfunctional

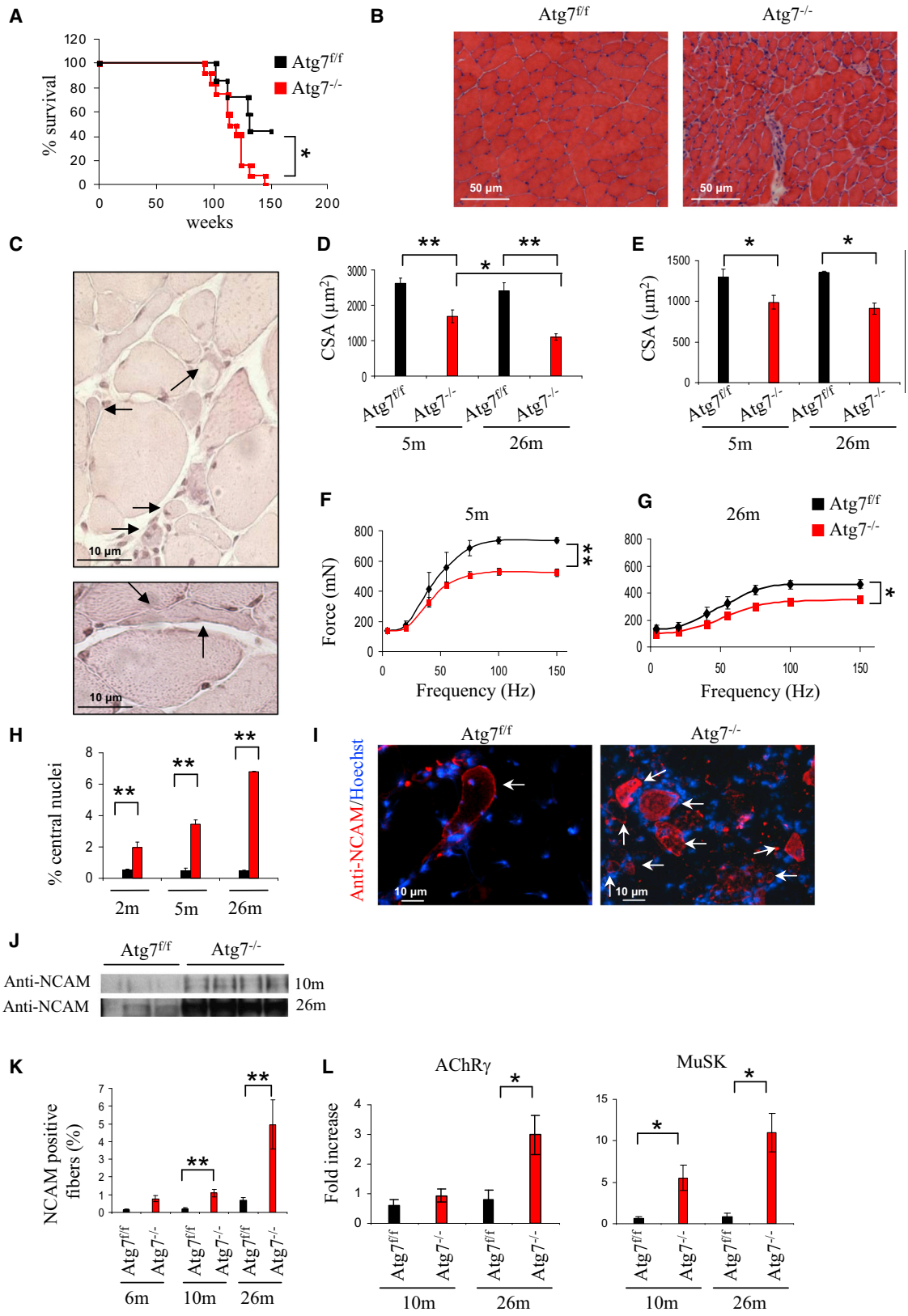

(legend on next page)

mitochondria that generate an enhancement of reactive oxygen species (ROS) production and oxidative stress. Over the past years, several researchers have reported that oxidative stress might be involved in etiology of weakness, NMJ degeneration, and sarcopenia (Jang et al., 2010, 2012). In fact, inhibition of autophagy induced an accumulation of mitochondria as revealed by succinate dehydrogenase (SDH) staining (Figure 6A). Electron microscopy analyses revealed the presence of giant mitochondria containing abnormal cristae (Figure 6B). The abnormal mitochondria are also dysfunctional. *Atg7*$^{-/-}$ flexor digitorum brevis (FDB) myofibers showed a significant increase of mitochondria that depolarized when the F_1F_0-ATPase was blocked by oligomycin (Grumati et al., 2010; Figure 6C). Similarly, FDB myofibers isolated from aged *Atg7*$^{f/f}$ showed a significant increase in depolarized mitochondria, which was corrected by restoring ATG7 expression (Figure S4A).

The alteration of mitochondrial morphology and function is associated with increased oxidative stress as revealed by protein carbonylation (Figure 6D). *Atg7*$^{-/-}$ muscles showed a 2-fold increase of carbonylated proteins when compared to age-matched controls. We performed a proteomic approach on carbonylated proteins and found that mitochondrial and sarcomeric proteins are more oxidized in *Atg7*$^{-/-}$ than controls (Table S1; Figure S4B). Because oxidative stress is believed to affect force generation, its enhancement might contribute to age-dependent weakness. Morphological and functional analyses on isolated single-skinned fibers confirmed that *Atg7*$^{-/-}$ myofibers are more atrophic and generate less force (Figures 6E and S4C). When the absolute force was normalized for myofiber size, the resulting specific force was still significantly lower (Figure 6F). Thus, not only the muscles became smaller, but there was a general impairment in force transmission, which led to profound weakness. The reduction of specific force may be caused by posttranslational modifications of contractile proteins induced by ROS. We then purified actin and myosin from *Atg7*$^{-/-}$ muscles and confirmed that both proteins were more oxidized in *Atg7*$^{-/-}$ mice (Figure 6G; Table S1). Acto-myosin function was investigated using an in vitro motility assay approach (Canepari et al., 2012). Actin sliding velocity on both myosin and heavy meromyosin fraction (HMM) of *Atg7*$^{-/-}$ was slower compared to controls (Figure 6H), confirming that an alteration of the functional properties of contractile proteins occurs when autophagy is reduced.

To test the role of oxidative stress in sarcopenia, we treated animals with Trolox, a potent antioxidant, for 4 weeks. The treatment successfully reduced the amount of total carbonylation on muscle protein extracts (Figures 7A and S4B; Table S1). Protein carbonylation of Trolox-treated *Atg7*$^{-/-}$ no longer differed from age-matched controls. The proteomic approach confirmed that Trolox abolished the oxidation of mitochondrial and sarcomeric proteins (Table S1; Figure S4B). Importantly, antioxidant treatment blocked the oligomycin-dependent mitochondrial depolarization of *Atg7*$^{-/-}$ mice (Figure 7B). We then addressed whether atrophy, weakness, and NMJ degeneration are affected by blunting oxidative stress. The treatment did not rescue myofiber size (Figures 7C and S5) but reduced the drop of specific force in isolated *Atg7*-deficient myofibers (Figure 7D). Trolox completely prevented carbonylation of purified myosin and actin (Figures 7E and S4B) and restored a normal acto-myosin function (Figure 7F). Looking at NMJ, we found that inhibition of ROS in adult *Atg7*$^{-/-}$ mice partially reduced NMJ instability whereas it did not give protection from NMJ fragmentation (Figure 7G). In conclusion, these findings strongly suggest that ROS production directly affects acto-myosin interaction and force generation but shows a limited involvement in the changes occurring at NMJ and no effect on atrophy.

DISCUSSION

The present study provides several important insights concerning the role of autophagy in NMJ preservation during aging. The most striking conclusion is that autophagy controls two important destabilizing factors that are (1) the removal of dysfunctional mitochondria that produce ROS and (2) the endosome recycling

Figure 2. Morphological and Functional Changes in Muscles of Atg7$^{-/-}$ during Aging

(A) Kaplan-Meier curve of *Atg7*$^{f/f}$ and *Atg7*$^{-/-}$ mice. *Atg7*$^{-/-}$ mice die earlier than their *Atg7*$^{f/f}$ counterparts. Comparison of *Atg7*$^{f/f}$ and *Atg7*$^{-/-}$ survival curves was performed by both Mantel-Cox and Gehan-Breslow-Wilcoxon tests. *Atg7*$^{-/-}$ mice show a significant reduction in the lifespan compared to controls (*$p < 0.05$).

(B) Morphological analyses of aged *Atg7*$^{f/f}$ and *Atg7*$^{-/-}$ tibialis anterior (TA) muscles. H&E staining shows that *Atg7*$^{-/-}$ muscles are atrophic with interstitial inflammation and center-nucleated fibers.

(C) Higher magnification of atrophic fibers of aged *Atg7*$^{-/-}$ mice showing angular, flat fibers and extremely small fibers (arrows).

(D) Quantification of the cross-sectional area (CSA) of glycolitic myofibers in TA muscles of adult and aged *Atg7*$^{f/f}$ and *Atg7*$^{-/-}$ mice. Values are mean ± SEM. At least four muscles of each group were analyzed; **$p < 0.01$; *$p < 0.05$.

(E) Quantification of CSA of oxidative myofibers of TA. Values are mean ± SEM; $n > 4$ for each group; *$p < 0.05$.

(F and G) Force measurements performed in vivo. (F) *Atg7*$^{-/-}$ mice show a profound decrease in maximal force generation in adult animals. Values are mean ± SEM ($n = 5$); **$p < 0.01$. (G) Aging reduces force production in both *Atg7*$^{f/f}$ and *Atg7*$^{-/-}$ mice, therefore aggravating the already profound weakness of *Atg7*$^{-/-}$ mice. Values are mean ± SEM; $n = 4$; *$p < 0.05$.

(H) Quantification of center-nucleated myofibers in TA ($n > 4$ for each group; **$p < 0.01$). Values are mean ± SEM.

(I) Representative images of immunostaining for NCAM expression in aged mice. Localization of NCAM along the entire fibers indicates the loss of muscle-nerve interaction.

(J) Immunoblotting for NCAM protein on muscle extracts from adult and aged gastrocnemius muscles. *Atg7*$^{-/-}$ muscles express higher levels of NCAM than age-matched *Atg7*$^{f/f}$.

(K) Quantification of NCAM-positive fibers. Values were normalized for the total number of myofibers in muscle section (at least four muscles of each group were analyzed; **$p < 0.01$). *Atg7*$^{-/-}$ mice are characterized by much-higher age-dependent increase in NCAM-positive fibers than age-matched *Atg7*$^{f/f}$. Values are mean ± SEM.

(L) Expression levels of acetylcholine receptor AChR γ-subunit (CHRNG) (left) and MuSK (right). MuSK and AChR are upregulated in adult and aged Atg7$^{-/-}$ muscles ($n > 5$; *$p < 0.05$). Values are mean ± SEM.

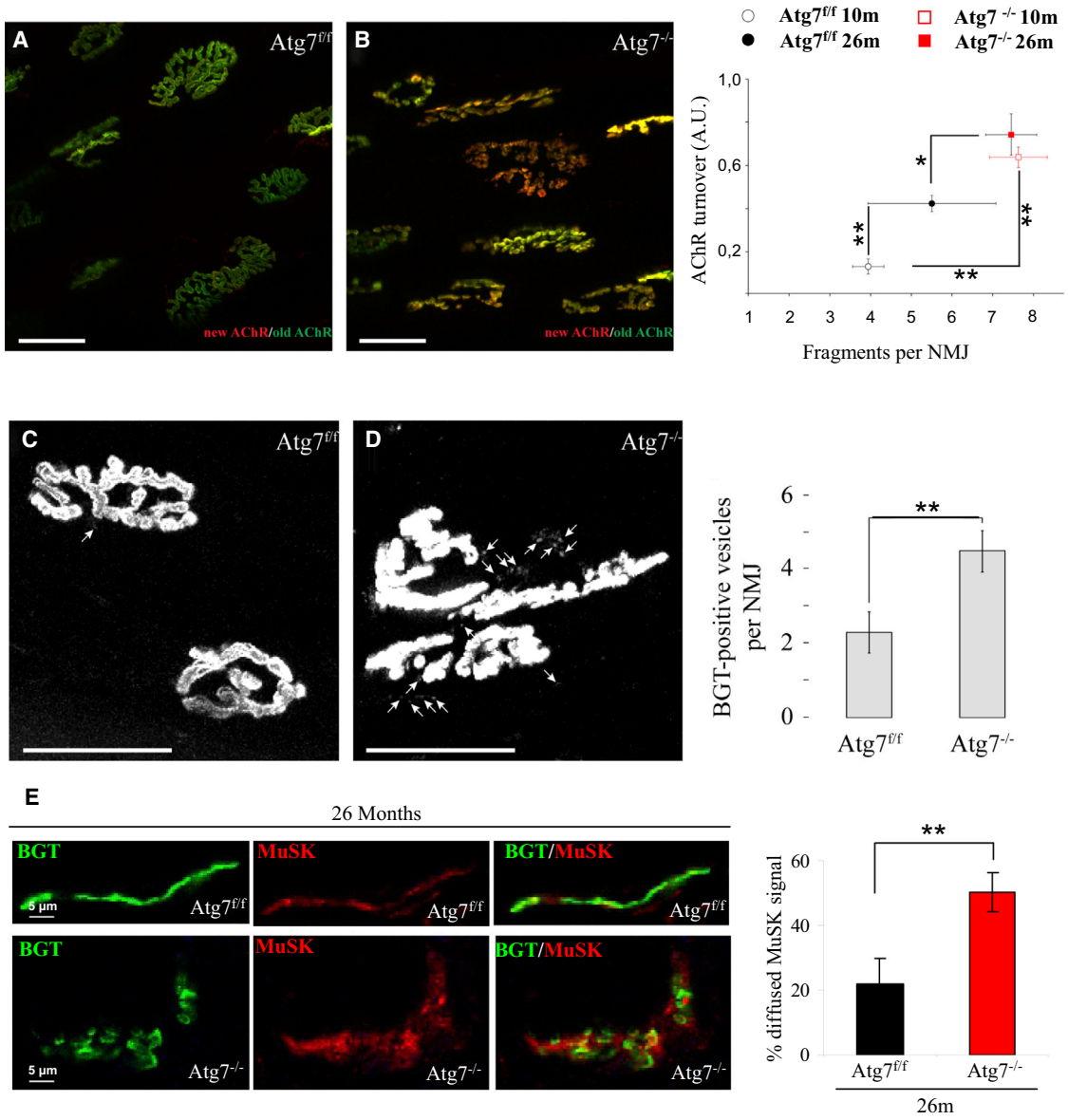

Figure 3. Neuromuscular Junctions of *Atg7*$^{-/-}$ Myofibers Are Unstable and Fragmented

(A and B) Representative images of *Atg7*$^{f/f}$ and *Atg7*$^{-/-}$ neuromuscular junctions (NMJ) obtained using confocal in vivo microscopy. Muscles were in vivo pulse labeled with bungarotoxins (BGTs) conjugated with different fluorophores. BGT-Alexa Fluor 647 (shown in green) was injected 10 days before microscopy, thus identifying stable AChR, whereas BGT-Alexa Fluor 555 (shown in red), injected 1 hr prior to microscopy, identifies newly incorporated AChR. Micrographs show representative maximum z projections of confocal in vivo images of NMJs from *Atg7*$^{f/f}$ (A) and *Atg7*$^{-/-}$ (B). The panel on the right shows the quantification of AChR turnover as a function of NMJ fragmentation of adult and aged *Atg7*$^{f/f}$ versus *Atg7*$^{-/-}$. Data are from at least four muscles of each group; $^{**}p < 0.01$; $^{*}p < 0.05$. A.U., arbitrary units. In the right panel of (B), values are mean ± SEM.

(C and D) Muscles were labeled with BGT-Alexa Fluor 555 48 hr before microscopy. In vivo confocal imaging was used to determine the amount of structures containing endocytic AChR. Micrographs show representative maximum z projections of confocal in vivo images of NMJs from *Atg7*$^{f/f}$ (C) and *Atg7*$^{-/-}$ (D). The panel on the right shows the average number of vesicular BGT-Alexa Fluor 555-positive structures per optical section. Data from 13 and 27 NMJs for *Atg7*$^{f/f}$ and *Atg7*$^{-/-}$, respectively; $^{**}p < 0.01$. In the right panel of (D), values are mean ± SEM.

(E) Immunohistochemistry of MuSK expression on aged *Atg7*$^{f/f}$ and *Atg7*$^{-/-}$ myofibers. Upper panel shows normal pattern of NMJs in *Atg7*$^{f/f}$ mice, where MuSK (red) localizes to NMJ, revealed by BGT-Alexa Fluor 647 (green). Lower panel shows MuSK (red) that accumulates inside myofibers at the level of NMJ (green). Panel on the right shows that the amount of diffused MuSK staining normalized over the total number of MuSK-positive NMJs is higher in aged *Atg7*$^{-/-}$ than *Atg7*$^{f/f}$; $^{**}p < 0.01$. In the right panel, values are mean ± SEM.

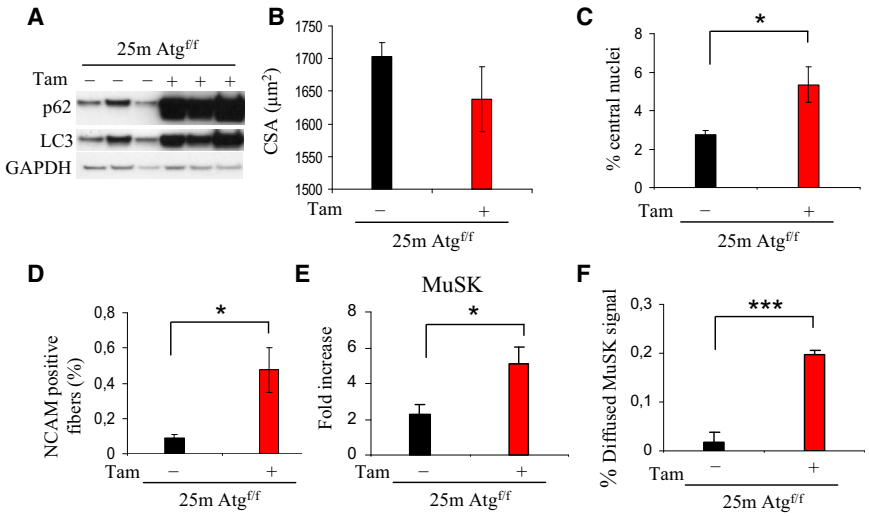

Figure 4. Acute Inhibition of Autophagy in Aged Mice Exacerbates Features of Sarcopenia and NMJ Degeneration

(A) Immunoblotting for LC3 and p62 proteins on muscle extracts from 25-month-old tamoxifen-inducible *Atg7*$^{-/-}$ female mice. Three months after the tamoxifen treatment, skeletal muscles were collected and analyzed.

(B) Acute inhibition of autophagy in old mice induces muscle degeneration. Quantification of the CSA of myofibers in TA muscles of aged tamoxifen-inducible *Atg7*$^{-/-}$ and *Atg7*$^{f/f}$ mice. Values are mean ± SEM; at least five muscles of each group were analyzed.

(C) Quantification of center-nucleated myofibers in TA of tamoxifen-inducible *Atg7*$^{-/-}$ ($n > 5$ for each group; *$p < 0.05$). Values are mean ± SEM.

(D) Acute inhibition of *Atg7* in aged female mice increases the number of denervated NCAM-positive fibers when compared to age-matched controls. Values were normalized for the total number of myofibers in muscle section (at least five muscles of each group were analyzed; *$p < 0.05$). Values are mean ± SEM.

(E) Expression levels of MuSK after acute inhibition of Atg7 in old mice. MuSK is upregulated in aged tamoxifen-inducible *Atg7*$^{-/-}$ muscles (*$p < 0.05$; $n > 5$). Values are mean ± SEM.

(F) Acute inhibition of autophagy in aged mice led to an increased amount of diffused MuSK staining; at least four muscles of each group were analyzed; ***$p < 0.001$. Values are mean ± SEM.

of AChR that affects MuSK localization and muscle-nerve interaction. The consequence of aging is the deterioration of tissue function mainly due to accumulation of damaged DNA, proteins, and organelles. Autophagy is a critical system to maintain the cell clear from dysfunctional organelles and mis- or unfolded proteins that are prone to aggregate and to preserve DNA stability (Sandri, 2010). Due to these actions and that autophagy declines with aging, there is consensus in considering autophagy as an antiaging system. Genetic evidence in flies and worms sustain this concept, but these data are still lacking in mammals. In fact, autophagy knockout mice die as newborns due to a general energy failure (Kuma et al., 2004), and most of the tissue-specific knockouts (Hara et al., 2006; Komatsu et al., 2006; Nakai et al., 2007) show severe organ dysfunction that precludes aging studies. Instead, our findings support the notion that autophagy failure contributes to aging.

Aging is a multisystemic disorder that affects multiple organs, leading to alterations of metabolism and tissue function. The postmitotic tissues such as brain, heart, and skeletal muscle are the most susceptible to age-related disease, and their dysfunction contributes importantly to precocious aging. The important role of muscle in healthy aging has been sustained by recent studies in *Drosophila*. Activation of autophagy by overexpression of FOXO transcription factor in the muscles of flies increases longevity (Demontis and Perrimon, 2010). The extension of lifespan is due to reduction of food intake and insulin release from neurosecretory cells, confirming that maintenance of a normal autophagy level in skeletal muscle, but not in adipose tissue, positively affects whole-body metabolism (Demontis and Perrimon, 2010). However, the role of autophagy in age-related muscle loss in mammals is still unclear, being either beneficial or detrimental (Gaugler et al., 2011; Wenz et al., 2009; Wohlgemuth et al., 2010). Our findings support the notion that autophagy is critical to prevent age-related denervation and weakness. Indeed, autophagy inhibition is sufficient to trigger a cascade of events that resemble those happening in elderly people.

Because mitochondria are the main producers of ROS, dysfunctional mitochondria are thought to play a key role in muscle function decline. In old age, a significant portion of mitochondria are abnormally enlarged, more rounded in shape, and display vacuolization in the matrix and shorter cristae (Peterson et al., 2012). Moreover, an increasing portion of them are also depolarized or nonfunctional. These features are present in autophagy-deficient muscles of adult animals, suggesting that defects in mitochondrial turnover are involved in age-dependent mitochondrial abnormalities. It is established that ROS production is increased in aged muscle in both the subsarcolemmal and intermyofibrillar pools of mitochondria (Chabi et al., 2008). This increase in ROS has been reported to induce oxidation of complex V, leading to decreased ATP production (Peterson et al., 2012). Accordingly, adult *Atg7*$^{-/-}$ muscles showed a significant increase of carbonylated ATP synthase (Table S1). Consistent with the ROS-mediated inhibition of ATP synthase, the energy-stress sensor of the cell, AMPK, is activated in *Atg7*-null muscles (not shown; Masiero et al., 2009). Our data show that mitochondrial dysfunction can be reversed by blocking ROS production. This finding is consistent with a recent report that showed improvement of age-related deficit, including mitochondrial function, by expressing a mitochondrial-targeted human catalase (Lee et al., 2010a).

Excessive ROS production does not only damage mitochondria but also cellular proteins. In muscle, oxidation of contractile proteins has been described, but the functional meaning of this condition is unclear. Our data establish that oxidative stress affects acto-myosin function and force generation. We showed

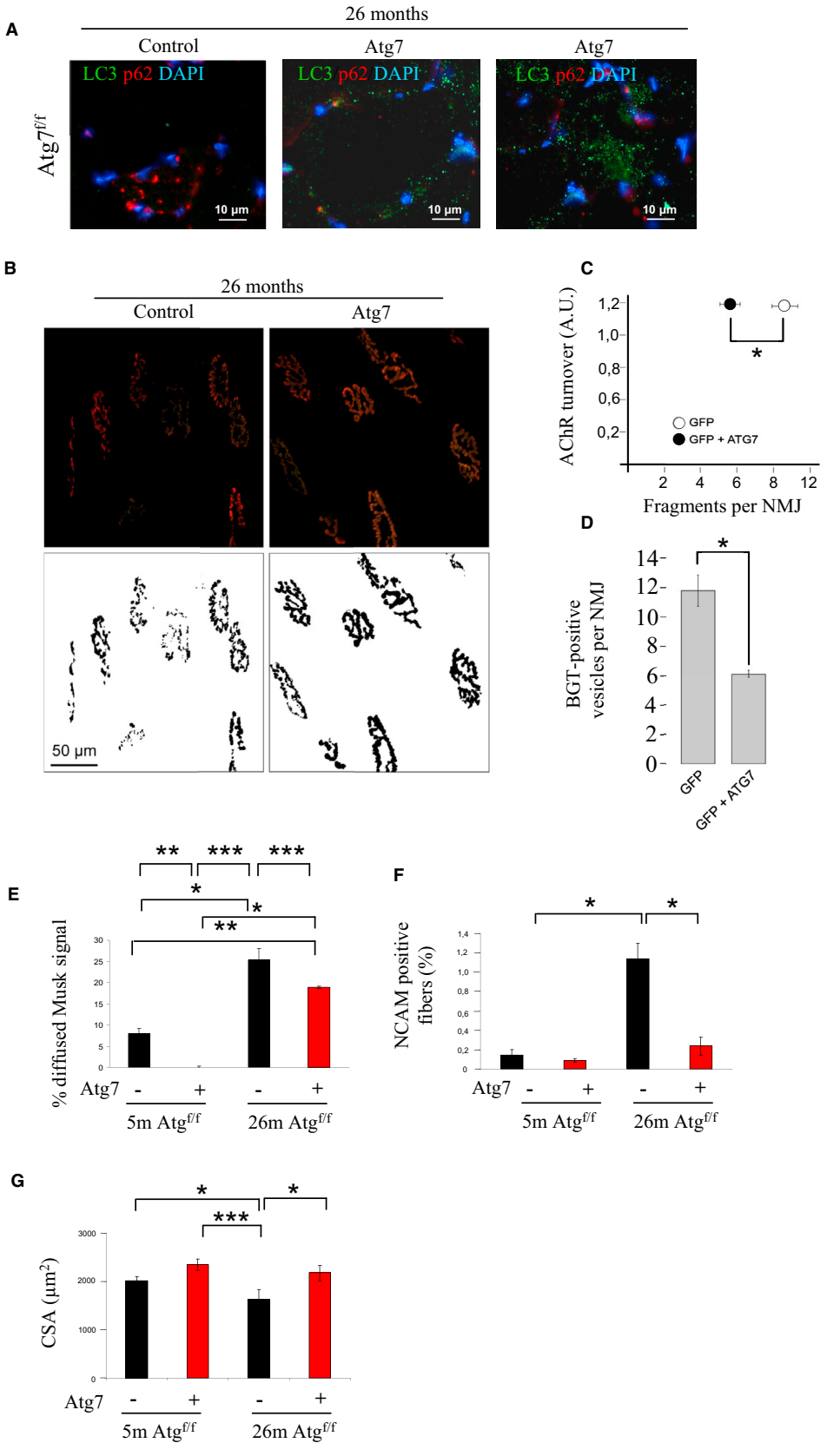

(legend on next page)

by proteomic analyses that contractile proteins are carbonylated and that Trolox treatment reverts both protein oxidation and the myosin capacity of moving actin filaments, ultimately improving muscle force. It is well established that changes in muscle mass and strength tend to be dissociated in elderly persons, the decline of muscle strength being three times faster than the decrease of muscle mass (Peterson et al., 2012). This suggests that alteration in the quality of contractile proteins plays a critical role during age-related decrease of muscle force. Accordingly, *Atg7*$^{-/-}$ myofibers show a significant decrease of force compared to age-matched controls, and this decline is corrected by Trolox. However, whereas the antioxidant improves acto-myosin function, it does not protect from muscle atrophy, although we cannot exclude that extending Trolox treatment for longer periods may successfully inhibit the signaling pathways controlling muscle atrophy. Previous studies reported that mitochondrial ROS production may contribute to NMJ instability (Dobrowolny et al., 2008; Jang et al., 2010, 2012). Overexpression of uncoupling protein (UCP1), specifically in skeletal muscle, is sufficient to dismantle NMJ and to induce distal motor neuron degeneration (Dupuis et al., 2009). Our data suggest that ROS partially contribute to NMJ instability. In fact, whereas Trolox treatment slightly reduced the turnover of old and new AChR, it did not prevent NMJ fragmentation.

In conclusion, our data strongly support the concept that autophagy in a postmitotic tissue is required for the correct interplay between muscle and nerve and for the quality control of mitochondria. Our findings also sustain the concept that the beneficial effects of caloric restriction and exercise on aging are a consequence of autophagy reactivation.

EXPERIMENTAL PROCEDURES

Animals, Human Biopsies, In Vivo Transfection, and RNAi Experiments

Animals were handled by specialized personnel under the control of inspectors of the Veterinary Service of the Local Sanitary Service (ASL 16—Padova), the local officers of the Ministry of Health. All procedures are specified in the projects approved by the Italian Ministero della Salute, Ufficio VI (authorization numbers C65). Subjects were male volunteers who received detailed information about the study and gave informed consent. Approval from the ethics committees of the City of Vienna and the Comenius University in Bratislava for medical ethics was obtained at the outset of the study. Muscle-specific Atg7-null (Atg7$^{-/-}$) and tamoxifen-inducible muscle-specific Atg7$^{-/-}$ mice have been previously described (Masiero et al., 2009). Tamoxifen-induced Cre LoxP recombination was activated by oral administration of tamoxifen-containing chow (Tam400/Cre ER Harlan). In vivo transfection and RNAi experiments were performed as previously described (Sandri et al., 2004). Sequences and plasmids are described in the Supplemental Experimental Procedures. For in vitro validation of shRNA constructs, C2C12 cells were maintained in Dulbecco's modified Eagle's medium (DMEM)/10% fetal bovine serum and transfected with shRNA constructs using Lipofectamine 2000 (Life Technologies). Cells were lysed and processed for gene expression analyses or western blot.

Measurements of Muscle Force In Vivo

Muscle force was measured in living animals as previously described (Blaauw et al., 2008).

Single-Fiber Dissection, Solutions, and Experimental Setup

The method used for single-muscle-fiber dissection, the solutions, and the experimental setup have been previously described (Bottinelli et al., 1996).

Single-Fiber Analysis

Single-fiber analysis was performed as previously described (Bottinelli et al., 1996). The experiments were performed at a temperature of 12°C. Sarcomere length was determined and set at 2.5 μm. The CSA of the fibers was determined without correction for swelling. Absolute (Po) and specific forces (Po/CSA) of the fibers were determined. At the end of the mechanical experiment, fibers were put in 20 μl of Laemmli buffer and stored at −20°C for subsequent electrophoretic analysis of myosin heavy chain (MHC) isoform content.

Contractile Proteins for In Vitro Motility Assay

Myosin Extraction from Bulk Muscles

Myosin isoform 2B was extracted from bulk gastrocnemius muscles of mice according to a procedure previously described in detail (Canepari et al., 2000) and used to prepare the HMM.

HMM Preparation

HMM was obtained by a proteolytic digestion with α-chimotrypsin of myosin according to a modification of the method of Margossian and Lowey (1982) previously described in detail (Canepari et al., 2000).

Actin Preparation

G-actin was extracted as described by Pardee and Spudich (1982) from acetone powder prepared from the residues of mice muscles after myosin extraction. After polymerization, F-actin was labeled by incubation for several hours with rhodamine-phalloidine (Molecular Probes R415) as described by Kron et al. (1991).

IVMA

Myosin (or HMM) was diluted to 0.1 mg/ml in a high (or low) ionic strength buffer and infused in a flow cell treated with nitrocellulose and prepared according to Anson et al. (1995). The in vitro motility assay (IVMA) analysis was performed according to Canepari et al. (2000) and Bottinelli et al. (1999) at 25°C. The composition of the experimental buffer was 3-(N-morpholino)

Figure 5. Rescue of Atg7 Expression in Aged Mice Improves Neuromuscular Synaptic Function

(A) Rescue of *Atg7* expression restores autophagosome formation in 26-month-old mice. TA muscles were transfected with *Atg7* expression plasmid, and 14 days later, TA were collected and stained for LC3 (green), p62 (red), and nuclei (blue).

(B) Confocal in vivo microscopy showing that rescue of ATG7 expression greatly reduces AChR fragmentation (data from at least four muscles per group; *$p < 0.05$) of aged *Atg7*$^{f/f}$ mice. Representative images are shown.

(C) Quantification of the AChR turnover as a function of NMJ fragmentation of aged *Atg7*$^{f/f}$. Restoring *Atg7* expression greatly improves NMJ fragmentation; n = 189 NMJs for *Atg7*$^{f/f}$ -GFP and 158 *Atg7*$^{f/f}$ GFP-ATG7; **$p < 0.01$. Values are mean ± SEM.

(D) Average number of vesicular BGT-Alexa Fluor 555-positive structures per optical section. Data from 189 NMJs for *Atg7*$^{f/f}$ -GFP and 158 *Atg7*$^{f/f}$ GFP-ATG7, respectively; *$p < 0.05$. Values are mean ± SEM.

(E) Rescue of Atg7 expression and autophagy in aged mice decreased the amount of diffused MuSK staining (at least three muscles of each group were analyzed; ***$p < 0.001$; **$p < 0.01$; *$p < 0.05$). Values are mean ± SEM.

(F) Restoring *Atg7* expression in aged mice improves the number of denervated NCAM-positive fibers when compared to age-matched controls and adult mice (three muscles of each group were analyzed; *$p < 0.05$). Values are mean ± SEM.

(G) Quantification of the CSA of myofibers in TA muscles of adult and aged *Atg7*$^{f/f}$ in presence or absence of *Atg7* expression. Values are mean ± SEM; at least three muscles of each group were analyzed; *$p < 0.05$.

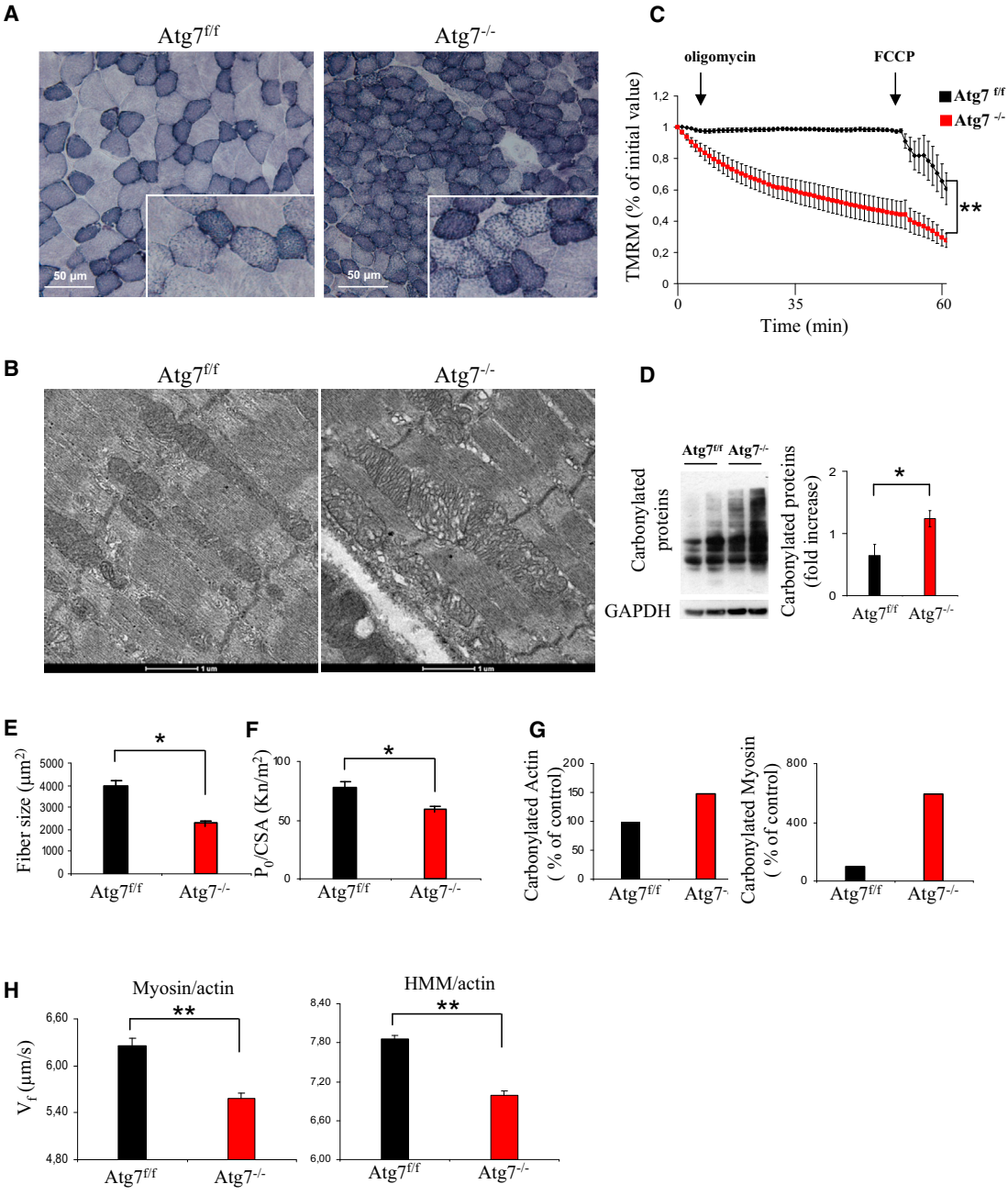

Figure 6. Autophagy Inhibition Induces Oxidative Stress and Mitochondrial Dysfunction

(A) SDH staining on serial sections of aged *Atg7*$^{f/f}$ and *Atg7*$^{-/-}$ muscles (TA) shows an accumulation of abnormal mitochondria in *Atg7*$^{-/-}$ myofibers.

(B) Electron microscopy images of extensor digitorum longus muscles from aged *Atg7*$^{f/f}$ and *Atg7*$^{-/-}$ mice show accumulation of abnormal mitochondria displaying alterations in size, cristae morphology, and matrix density.

(C) Measurement of mitochondrial membrane potential. TMRM staining was monitored in at least 20 fibers per group (**$p < 0.001$). Values are mean ± SEM.

(D) Overall protein carbonylation of aged *Atg7*$^{f/f}$ and *Atg7*$^{-/-}$ muscles, revealed by Oxyblot. A representative immunoblot for carbonylated proteins is depicted on the left, and densitometric quantification of the carbonylated proteins is in the graph on the right. Aged *Atg7*$^{-/-}$ mice show higher ongoing protein carbonylation than *Atg7*$^{f/f}$ ($n = 5$; *$p < 0.05$). Values are mean ± SEM.

(E and F) In vitro analysis of isolated skinned muscle fibers from gastrocnemius muscles of *Atg7*$^{f/f}$ and *Atg7*$^{-/-}$. (E) Single *Atg7*$^{-/-}$ myofibers are more atrophic (E) and weaker (F) than *Atg7*$^{f/f}$ counterparts (at least 20 fibers for each condition; *$p < 0.05$). Values are mean ± SEM.

(G) Carbonylation of the pooled actin (on the left) and myosin (on the right) proteins, extracted from *Atg7*$^{f/f}$ and *Atg7*$^{-/-}$ GCN and used for in vitro motility assay. *Atg7*$^{-/-}$ show higher carbonylation than *Atg7*$^{f/f}$.

(H) In vitro motility assay reveals reduced actin sliding velocity (*Vf*) on myosin (left panel) and HMM (right panel) extracted from adult *Atg7*$^{-/-}$ muscles in comparison with *Atg7*$^{f/f}$. Reduced actin sliding velocity was statistically significant in *Atg7*$^{-/-}$ ($n = 4$ of each condition; **$p < 0.01$) on both myosin and HMM. Values are mean ± SEM.

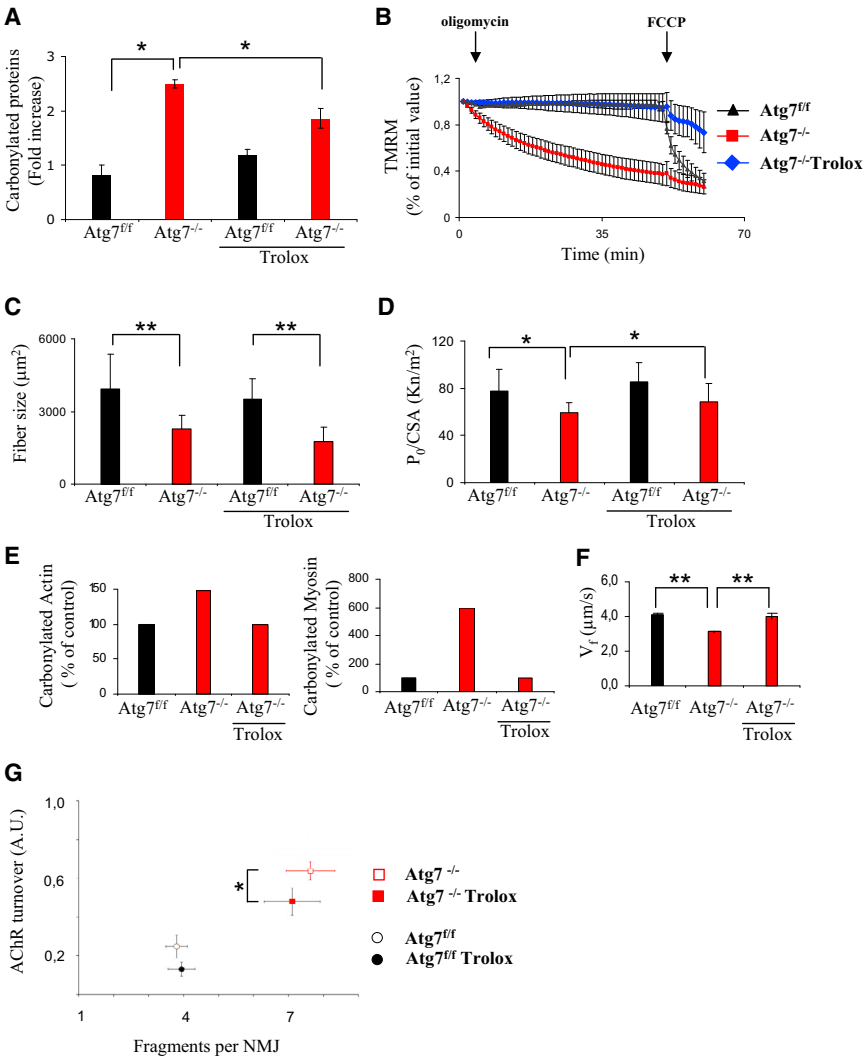

Figure 7. Inhibition of Oxidative Stress Restores the Ability of Mitochondria to Maintain Membrane Potential and the Functionality of Actin-Myosin Complex but Shows Limited Effect on NMJ

(A) Trolox treatment reduces the level of overall protein carbonylation in *Atg7*$^{-/-}$ muscles, thus abolishing the difference with *Atg7*$^{f/f}$ (n = 4 mice per condition; *p < 0.05). Values are mean ± SEM.

(B) Trolox treatment restores the ability of *Atg7*$^{-/-}$ mitochondria to maintain membrane potential (n > 20 fibers per group; **p < 0.001). Values are mean ± SEM.

(C) Trolox treatment does not affect fiber size in both *Atg7*$^{f/f}$ and *Atg7*$^{-/-}$ muscles (n = 4 mice per condition; **p < 0.01). Values are mean ± SEM.

(D) In vitro isolated skinned fiber analysis: Trolox treatment rescues the specific muscle force of isolated *Atg7*$^{-/-}$ myofibers; data re-expressed as mean ± SD; n = 4 mice per condition; *p < 0.05.

(E) Trolox treatment reduces the level of actin (left panel) and myosin (right panel) protein carbonylation in *Atg7*$^{-/-}$ muscles, thus abolishing the difference with *Atg7*$^{f/f}$; n = 4 samples. Values are mean ± SEM.

(F) Trolox treatment rescues actin sliding velocity (*Vf*) in adult *Atg7*$^{-/-}$ muscles in in vitro motility assay; n = 4 mice per condition; **p < 0.01. Values are mean ± SEM.

(G) Confocal in vivo microscopy showing that Trolox treatment slightly reduces AChR turnover (data from at least four muscles per group; *p < 0.05) but does not have any effect on NMJ fragmentation of adult *Atg7*$^{f/f}$ and *Atg7*$^{-/-}$ mice. Values are mean ± SEM.

propanesulfonic acid 25 mM (pH = 7.4 at 25°C), KCl 25 mM, $MgCl_2$ 4 mM, EGTA 1 mM, dithiothreitol (DTT) 1 mM, glucose oxidase 200 μg/ml, catalase 36 μg/ml, glucose 5 mg/ml, and ATP 2 mM. Average velocities of actin filaments were determined. For each myosin and HMM sample, the velocities of at least 50 filaments were measured and their distribution characterized according to parametric statistics.

Gene-Expression Analyses

Total RNA was prepared from TA muscles using Trizol Reagent (Life Technologies). Complementary DNA generated with Life Technologies SuperScript III Reverse Transcriptase was analyzed by quantitative real-time PCR using Power SYBR Green Applied Biosystem. All data were normalized to glyceraldehyde 3-phosphate dehydrogenase. The oligonucleotide primers used are shown in Supplemental Experimental Procedures.

Immunoblotting

Cryosections of frozen gastrocnemius muscles were lysed in a buffer containing 50 mM Tris (pH 7.5), 150 mM NaCl, 10 mM MgCl2, 0.5 mM DTT, 1 mM EDTA, 10% glycerol, 2% SDS, 1% Triton X-100, Roche Complete Protease Inhibitor Cocktail, and Sigma Protease Inhibitor Cocktail. The samples were immunoblotted as previously described (Sandri et al., 2004) and visualized with SuperSignal West Pico Chemiluminescent substrate (Pierce). A list of antibodies is shown in the Supplemental Experimental Procedures.

Protein Carbonyls Detection and Antioxidant Treatment

Carbonylation of muscle proteins was detected by using the OxyBlot Protein Oxidation Detection Kit from Millipore (Masiero et al., 2009). Mice were intraperitoneally injected with Trolox (6-hydroxy-2,5,7,8-tetramethylchroman-2-carboxylic acid) 30 mg/kg daily for 4 weeks. For a detailed description of the detection of oxidized proteins, see the Supplemental Experimental Procedures.

2D OxyBlot Data Acquisition and Analysis

Spot detection and quantification was carried out using the Image Master 2D Platinum 7 software (GE Healthcare). For a detailed description of the procedure, see the Supplemental Experimental Procedures.

In-Gel Digestion, Mass Spectrometry Protein Identification, and Database Searches

For a detailed description of the procedure, see the Supplemental Experimental Procedures.

Histology, Fluorescence Microscopy, and Electron Microscopy

Cryosections of TA were stained for hematoxylin and eosin (H&E) and SDH. Immunofluorescence staining was performed on cryostatic sections as previously described (Masiero et al., 2009) and then monitored with a fluorescence microscope or confocal microscopy. Antibodies are described in the Supplemental Experimental Procedures. Fiber cross-sectional area was performed on TA or gastrocnemius (GCN) as described (Mammucari et al., 2007) and measured using ImageJ software. For electron microscopy, we used

conventional fixation-embedding procedures based on glutaraldehyde-osmium fixation and Epon embedding.

Cell Culture and Transient Transfections

C2C12 myogenic cell lines were cultured in DMEM (GIBCO-Life Technologies) supplemented with 10% fetal bovine serum. Myoblasts were transfected using Lipofectamine 2000 (Life Technologies) according to the manufacturer's instructions.

Single-Fiber Mitochondrial Membrane Potential Analyses

Mitochondrial membrane potential was measured in isolated transfected fibers from FDB muscles. Mitochondrial membrane potential was measured by epifluorescence microscopy based on the accumulation of tetramethylrhodamine, methyl ester (TMRM) fluorescence as previously described (Romanello et al., 2010).

MHC Identification

The MHC isoform composition of gastrocnemius muscles of mice was assessed by 8% SDS polyacrylammide gel electrophoresis as described by Pellegrino et al. (2003).

In Vivo Microscopy and Analysis of AChR Turnover and NMJ Fragmentation

In vivo microscopy of mice was performed under anesthesia using Zoletil and xylazine on a Leica SP2 confocal microscope equipped with a 63× 1.2 numerical aperture water immersion objective, essentially as described previously (Röder et al., 2008, 2010). Automated analysis of AChR turnover and NMJ fragmentation used algorithms described earlier (Röder et al., 2010).

Statistical Analysis and General Experimental Design

The sample size was calculated using size power analysis methods for a priori determination, based on the SD and effect size previously obtained using the experimental methods employed in the study. For animal studies, we estimated sample size from the expected number of knockout mice and littermate controls, which was based on Mendelian ratios. We calculated the minimal sample size for each group by at least four organisms. Considering a likely drop-off effect of 10%, we set the sample size of each group at five mice. To reduce the SD, we minimized physiological variation by using homogenous animals with the same sex and age. The exclusion criteria for animals were preestablished. In case of death, cannibalism, or sickness, the animal was excluded from analysis. Tissue samples were excluded in cases such as cryo-artifacts, histological artifacts, or failed RNA extraction. We included animals from different breeding cages by random allocation to the different experimental groups. Animal experiments were not blinded; however, when applicable, the experimenters were blinded to the nature of samples by using number codes until final data analysis was performed. Statistical tests were used as described in the figure legends and were applied upon verification of the test assumptions (e.g., normality). Generally, data were analyzed by Student's t test. For all graphs, data are represented as means ± SEM.

SUPPLEMENTAL INFORMATION

Supplemental Information includes Supplemental Experimental Procedures, five figures, and one table and can be found with this article online at http://dx.doi.org/10.1016/j.celrep.2014.07.061.

ACKNOWLEDGMENTS

This work was supported by Telethon-Italy (TCP04009), by the European Union (MYOAGE; contract: 223576 of FP7), by ERC (282310-MyoPHAGY), by the Italian Ministry of Education (MiUR) (PRIN 2010/2011), by the Leducq Foundation, and by CARIPARO to M.S. M.A.B. is currently the recipient of a postdoctoral fellowship from the Association Française contre les Myopathies (AFM). The authors also thank the 3P5 proteomics platform, Université Paris Descartes, Sorbonne Paris Cité, for the mass-spectrometry-based protein identifications.

Received: April 9, 2013
Revised: February 4, 2014
Accepted: July 31, 2014
Published: August 28, 2014

REFERENCES

Anson, M., Drummond, D.R., Geeves, M.A., Hennessey, E.S., Ritchie, M.D., and Sparrow, J.C. (1995). Actomyosin kinetics and in vitro motility of wild-type Drosophila actin and the effects of two mutations in the Act88F gene. Biophys. J. *68*, 1991–2003.

Blaauw, B., Mammucari, C., Toniolo, L., Agatea, L., Abraham, R., Sandri, M., Reggiani, C., and Schiaffino, S. (2008). Akt activation prevents the force drop induced by eccentric contractions in dystrophin-deficient skeletal muscle. Hum. Mol. Genet. *17*, 3686–3696.

Bottinelli, R., Canepari, M., Pellegrino, M.A., and Reggiani, C. (1996). Force-velocity properties of human skeletal muscle fibres: myosin heavy chain isoform and temperature dependence. J. Physiol. *495*, 573–586.

Bottinelli, R., Pellegrino, M.A., Canepari, M., Rossi, R., and Reggiani, C. (1999). Specific contributions of various muscle fibre types to human muscle performance: an in vitro study. J. Electromyogr. Kinesiol. *9*, 87–95.

Canepari, M., Rossi, R., Pellegrino, M.A., Bottinelli, R., Schiaffino, S., and Reggiani, C. (2000). Functional diversity between orthologous myosins with minimal sequence diversity. J. Muscle Res. Cell Motil. *21*, 375–382.

Canepari, M., Maffei, M., Longa, E., Geeves, M., and Bottinelli, R. (2012). Actomyosin kinetics of pure fast and slow rat myosin isoforms studied by in vitro motility assay approach. Exp. Physiol. *97*, 873–881.

Chabi, B., Ljubicic, V., Menzies, K.J., Huang, J.H., Saleem, A., and Hood, D.A. (2008). Mitochondrial function and apoptotic susceptibility in aging skeletal muscle. Aging Cell *7*, 2–12.

Chai, R.J., Vukovic, J., Dunlop, S., Grounds, M.D., and Shavlakadze, T. (2011). Striking denervation of neuromuscular junctions without lumbar motoneuron loss in geriatric mouse muscle. PLoS ONE *6*, e28090.

Demontis, F., and Perrimon, N. (2010). FOXO/4E-BP signaling in Drosophila muscles regulates organism-wide proteostasis during aging. Cell *143*, 813–825.

Dobrowolny, G., Aucello, M., Rizzuto, E., Beccafico, S., Mammucari, C., Boncompagni, S., Belia, S., Wannenes, F., Nicoletti, C., Del Prete, Z., et al. (2008). Skeletal muscle is a primary target of SOD1G93A-mediated toxicity. Cell Metab. *8*, 425–436.

Dupuis, L., Gonzalez de Aguilar, J.L., Echaniz-Laguna, A., Eschbach, J., Rene, F., Oudart, H., Halter, B., Huze, C., Schaeffer, L., Bouillaud, F., and Loeffler, J.P. (2009). Muscle mitochondrial uncoupling dismantles neuromuscular junction and triggers distal degeneration of motor neurons. PLoS ONE *4*, e5390.

Gaugler, M., Brown, A., Merrell, E., DiSanto-Rose, M., Rathmacher, J.A., and Reynolds, T.H., 4th. (2011). PKB signaling and atrogene expression in skeletal muscle of aged mice. J. Appl. Physiol. *111*, 192–199.

Grumati, P., Coletto, L., Sabatelli, P., Cescon, M., Angelin, A., Bertaggia, E., Blaauw, B., Urciuolo, A., Tiepolo, T., Merlini, L., et al. (2010). Autophagy is defective in collagen VI muscular dystrophies, and its reactivation rescues myofiber degeneration. Nat. Med. *16*, 1313–1320.

Grumati, P., Coletto, L., Sandri, M., and Bonaldo, P. (2011a). Autophagy induction rescues muscular dystrophy. Autophagy *7*, 426–428.

Grumati, P., Coletto, L., Schiavinato, A., Castagnaro, S., Bertaggia, E., Sandri, M., and Bonaldo, P. (2011b). Physical exercise stimulates autophagy in normal skeletal muscles but is detrimental for collagen VI-deficient muscles. Autophagy *7*, 1415–1423.

Hara, T., Nakamura, K., Matsui, M., Yamamoto, A., Nakahara, Y., Suzuki-Migishima, R., Yokoyama, M., Mishima, K., Saito, I., Okano, H., and Mizushima, N. (2006). Suppression of basal autophagy in neural cells causes neurodegenerative disease in mice. Nature *441*, 885–889.

He, C., Bassik, M.C., Moresi, V., Sun, K., Wei, Y., Zou, Z., An, Z., Loh, J., Fisher, J., Sun, Q., et al. (2012). Exercise-induced BCL2-regulated autophagy is required for muscle glucose homeostasis. Nature *481*, 511–515.

Jang, Y.C., and Van Remmen, H. (2011). Age-associated alterations of the neuromuscular junction. Exp. Gerontol. *46*, 193–198.

Jang, Y.C., Lustgarten, M.S., Liu, Y., Muller, F.L., Bhattacharya, A., Liang, H., Salmon, A.B., Brooks, S.V., Larkin, L., Hayworth, C.R., et al. (2010). Increased superoxide in vivo accelerates age-associated muscle atrophy through mitochondrial dysfunction and neuromuscular junction degeneration. FASEB J. *24*, 1376–1390.

Jang, Y.C., Liu, Y., Hayworth, C.R., Bhattacharya, A., Lustgarten, M.S., Muller, F.L., Chaudhuri, A., Qi, W., Li, Y., Huang, J.Y., et al. (2012). Dietary restriction attenuates age-associated muscle atrophy by lowering oxidative stress in mice even in complete absence of CuZnSOD. Aging Cell *11*, 770–782.

Kenyon, C.J. (2010). The genetics of ageing. Nature *464*, 504–512.

Komatsu, M., Waguri, S., Chiba, T., Murata, S., Iwata, J., Tanida, I., Ueno, T., Koike, M., Uchiyama, Y., Kominami, E., and Tanaka, K. (2006). Loss of autophagy in the central nervous system causes neurodegeneration in mice. Nature *441*, 880–884.

Kron, S.J., Toyoshima, Y.Y., Uyeda, T.Q., and Spudich, J.A. (1991). Assays for actin sliding movement over myosin-coated surfaces. Methods Enzymol. *196*, 399–416.

Kuma, A., Hatano, M., Matsui, M., Yamamoto, A., Nakaya, H., Yoshimori, T., Ohsumi, Y., Tokuhisa, T., and Mizushima, N. (2004). The role of autophagy during the early neonatal starvation period. Nature *432*, 1032–1036.

Lee, H.Y., Choi, C.S., Birkenfeld, A.L., Alves, T.C., Jornayvaz, F.R., Jurczak, M.J., Zhang, D., Woo, D.K., Shadel, G.S., Ladiges, W., et al. (2010a). Targeted expression of catalase to mitochondria prevents age-associated reductions in mitochondrial function and insulin resistance. Cell Metab. *12*, 668–674.

Lee, J.H., Budanov, A.V., Park, E.J., Birse, R., Kim, T.E., Perkins, G.A., Ocorr, K., Ellisman, M.H., Bodmer, R., Bier, E., and Karin, M. (2010b). Sestrin as a feedback inhibitor of TOR that prevents age-related pathologies. Science *327*, 1223–1228.

Mammucari, C., Milan, G., Romanello, V., Masiero, E., Rudolf, R., Del Piccolo, P., Burden, S.J., Di Lisi, R., Sandri, C., Zhao, J., et al. (2007). FoxO3 controls autophagy in skeletal muscle in vivo. Cell Metab. *6*, 458–471.

Mammucari, C., Schiaffino, S., and Sandri, M. (2008). Downstream of Akt: FoxO3 and mTOR in the regulation of autophagy in skeletal muscle. Autophagy *4*, 524–526.

Margossian, S.S., and Lowey, S. (1982). Preparation of myosin and its subfragments from rabbit skeletal muscle. Methods Enzymol. *85* (Pt B), 55–71.

Masiero, E., Agatea, L., Mammucari, C., Blaauw, B., Loro, E., Komatsu, M., Metzger, D., Reggiani, C., Schiaffino, S., and Sandri, M. (2009). Autophagy is required to maintain muscle mass. Cell Metab. *10*, 507–515.

Meléndez, A., Tallóczy, Z., Seaman, M., Eskelinen, E.L., Hall, D.H., and Levine, B. (2003). Autophagy genes are essential for dauer development and life-span extension in C. elegans. Science *301*, 1387–1391.

Mizushima, N., and Komatsu, M. (2011). Autophagy: renovation of cells and tissues. Cell *147*, 728–741.

Morrison, J.H., and Hof, P.R. (1997). Life and death of neurons in the aging brain. Science *278*, 412–419.

Nakai, A., Yamaguchi, O., Takeda, T., Higuchi, Y., Hikoso, S., Taniike, M., Omiya, S., Mizote, I., Matsumura, Y., Asahi, M., et al. (2007). The role of autophagy in cardiomyocytes in the basal state and in response to hemodynamic stress. Nat. Med. *13*, 619–624.

Pardee, J.D., and Spudich, J.A. (1982). Purification of muscle actin. Methods Enzymol. *85* (Pt B), 164–181.

Pellegrino, M.A., Canepari, M., Rossi, R., D'Antona, G., Reggiani, C., and Bottinelli, R. (2003). Orthologous myosin isoforms and scaling of shortening velocity with body size in mouse, rat, rabbit and human muscles. J. Physiol. *546*, 677–689.

Peterson, C.M., Johannsen, D.L., and Ravussin, E. (2012). Skeletal muscle mitochondria and aging: a review. J. Aging Res. *2012*, 194821.

Röder, I.V., Petersen, Y., Choi, K.R., Witzemann, V., Hammer, J.A., 3rd, and Rudolf, R. (2008). Role of Myosin Va in the plasticity of the vertebrate neuromuscular junction in vivo. PLoS ONE *3*, e3871.

Röder, I.V., Choi, K.R., Reischl, M., Petersen, Y., Diefenbacher, M.E., Zaccolo, M., Pozzan, T., and Rudolf, R. (2010). Myosin Va cooperates with PKA RIalpha to mediate maintenance of the endplate in vivo. Proc. Natl. Acad. Sci. USA *107*, 2031–2036.

Romanello, V., Guadagnin, E., Gomes, L., Roder, I., Sandri, C., Petersen, Y., Milan, G., Masiero, E., Del Piccolo, P., Foretz, M., et al. (2010). Mitochondrial fission and remodelling contributes to muscle atrophy. EMBO J. *29*, 1774–1785.

Rubinsztein, D.C., Mariño, G., and Kroemer, G. (2011). Autophagy and aging. Cell *146*, 682–695.

Sandri, M. (2010). Autophagy in skeletal muscle. FEBS Lett. *584*, 1411–1416.

Sandri, M., Sandri, C., Gilbert, A., Skurk, C., Calabria, E., Picard, A., Walsh, K., Schiaffino, S., Lecker, S.H., and Goldberg, A.L. (2004). Foxo transcription factors induce the atrophy-related ubiquitin ligase atrogin-1 and cause skeletal muscle atrophy. Cell *117*, 399–412.

Simonsen, A., Cumming, R.C., Brech, A., Isakson, P., Schubert, D.R., and Finley, K.D. (2008). Promoting basal levels of autophagy in the nervous system enhances longevity and oxidant resistance in adult Drosophila. Autophagy *4*, 176–184.

Valdez, G., Tapia, J.C., Kang, H., Clemenson, G.D., Jr., Gage, F.H., Lichtman, J.W., and Sanes, J.R. (2010). Attenuation of age-related changes in mouse neuromuscular synapses by caloric restriction and exercise. Proc. Natl. Acad. Sci. USA *107*, 14863–14868.

Visser, M., and Schaap, L.A. (2011). Consequences of sarcopenia. Clin. Geriatr. Med. *27*, 387–399.

Wenz, T., Rossi, S.G., Rotundo, R.L., Spiegelman, B.M., and Moraes, C.T. (2009). Increased muscle PGC-1alpha expression protects from sarcopenia and metabolic disease during aging. Proc. Natl. Acad. Sci. USA *106*, 20405–20410.

Wohlgemuth, S.E., Seo, A.Y., Marzetti, E., Lees, H.A., and Leeuwenburgh, C. (2010). Skeletal muscle autophagy and apoptosis during aging: effects of calorie restriction and life-long exercise. Exp. Gerontol. *45*, 138–148.

Zampieri, S., Pietrangelo, L., Loefler, S., Fruhmann, H., Vogelauer, M., Burggraf, S., Pond, A., Grim-Stieger, M., Cvecka, J., Sedliak, M., et al. (2014). Lifelong Physical Exercise Delays Age-Associated Skeletal Muscle Decline. J. Gerontol. A Biol. Sci. Med. Sci..

Zhao, J., Brault, J.J., Schild, A., Cao, P., Sandri, M., Schiaffino, S., Lecker, S.H., and Goldberg, A.L. (2007). FoxO3 coordinately activates protein degradation by the autophagic/lysosomal and proteasomal pathways in atrophying muscle cells. Cell Metab. *6*, 472–483.

Cell Reports, Volume *8*

Supplemental Information

Autophagy Impairment in Muscle Induces Neuromuscular Junction Degeneration and Precocious Aging

Silvia Carnio, Francesca LoVerso, Martin Andres Baraibar, Emanuela Longa, Muzamil Majid Khan, Manuela Maffei, Markus Reischl, Monica Canepari, Stefan Loefler, Helmut Kern, Bert Blaauw, Bertrand Friguet, Roberto Bottinelli, Rüdiger Rudolf, and Marco Sandri

SUPPLEMENTAL DATA

Supplemental Figures

Figure S1

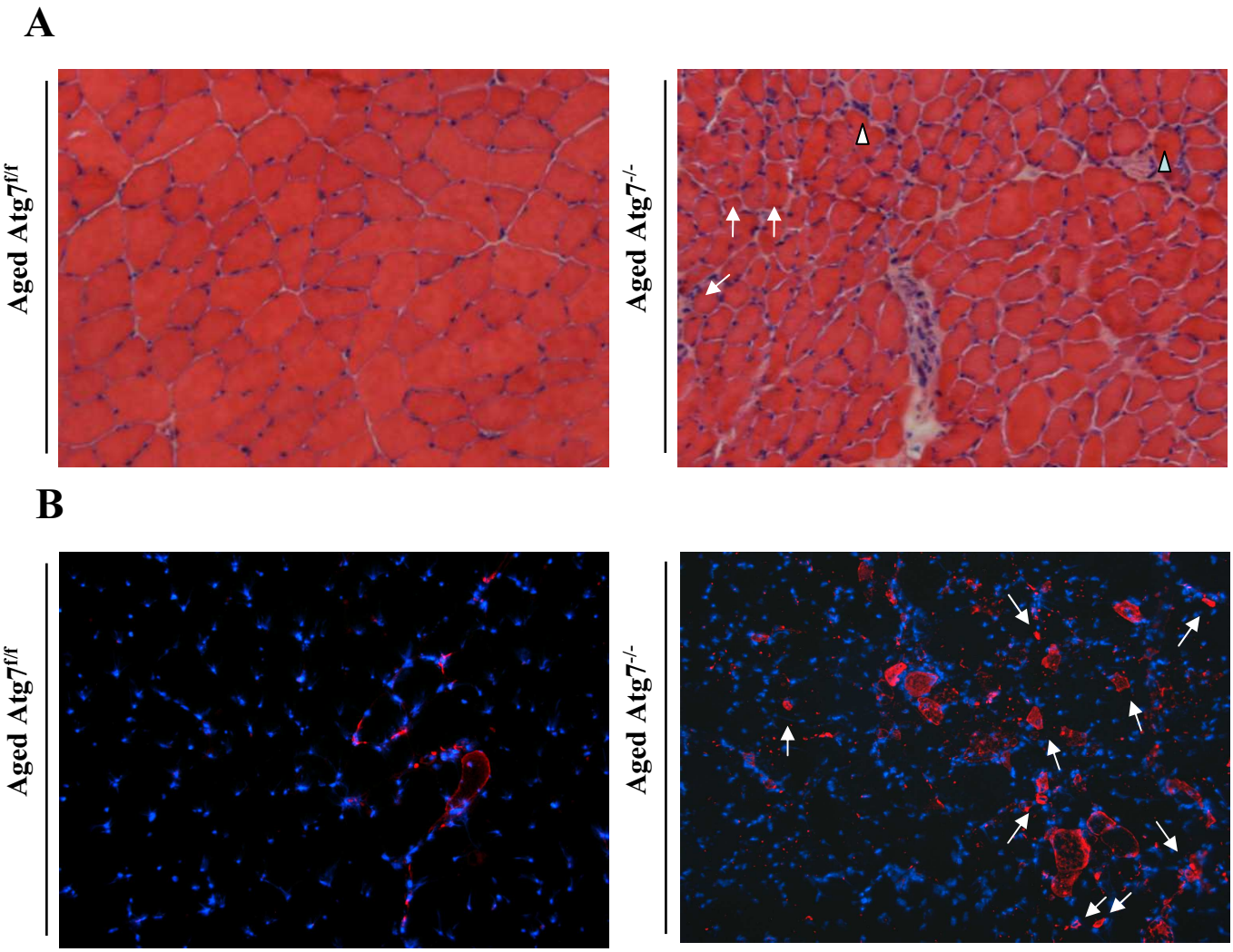

Figure S2

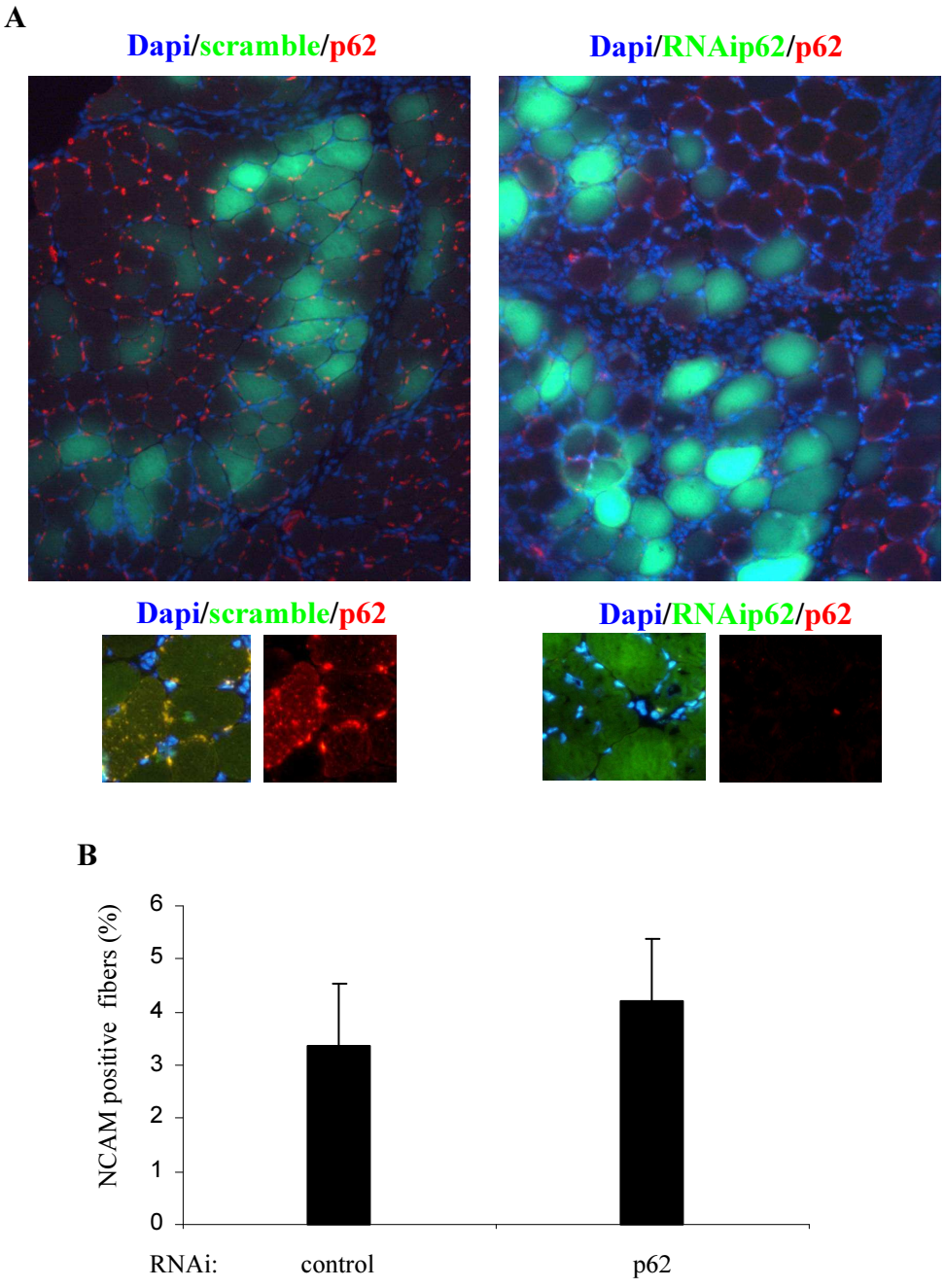
A
Dapi/scramble/p62
Dapi/RNAip62/p62
Dapi/scramble/p62
Dapi/RNAip62/p62
B
NCAM positive fibers (%)
0
1
2
3
4
5
6
RNAi:
control
p62

Figure S3

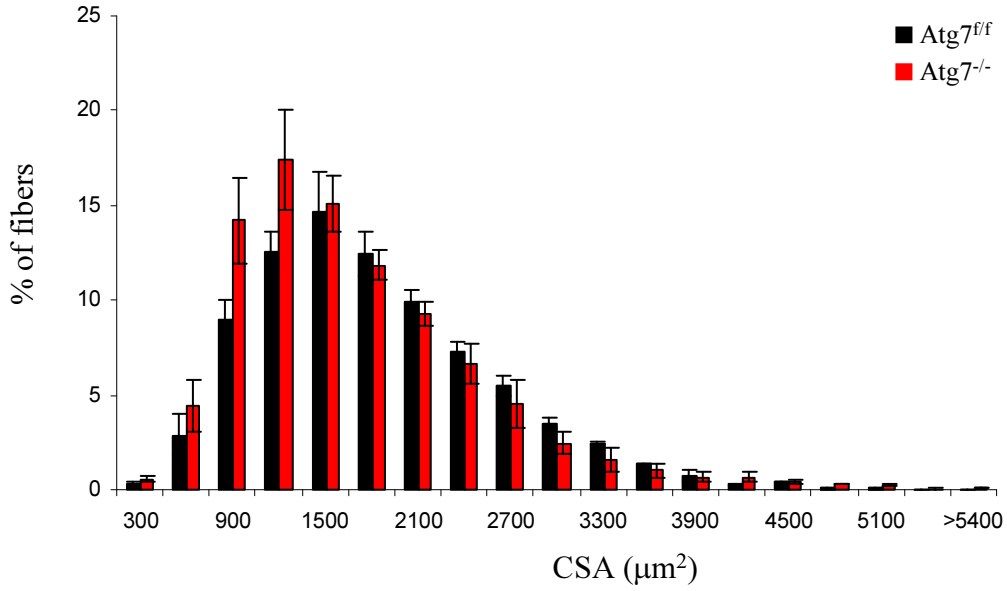
25
20
15
10
5
0
% of fibers
Atg7f/f
Atg7-/-
300
900
1500
2100
2700
3300
3900
4500
5100
>5400
CSA (µm2)

Figure S4

A

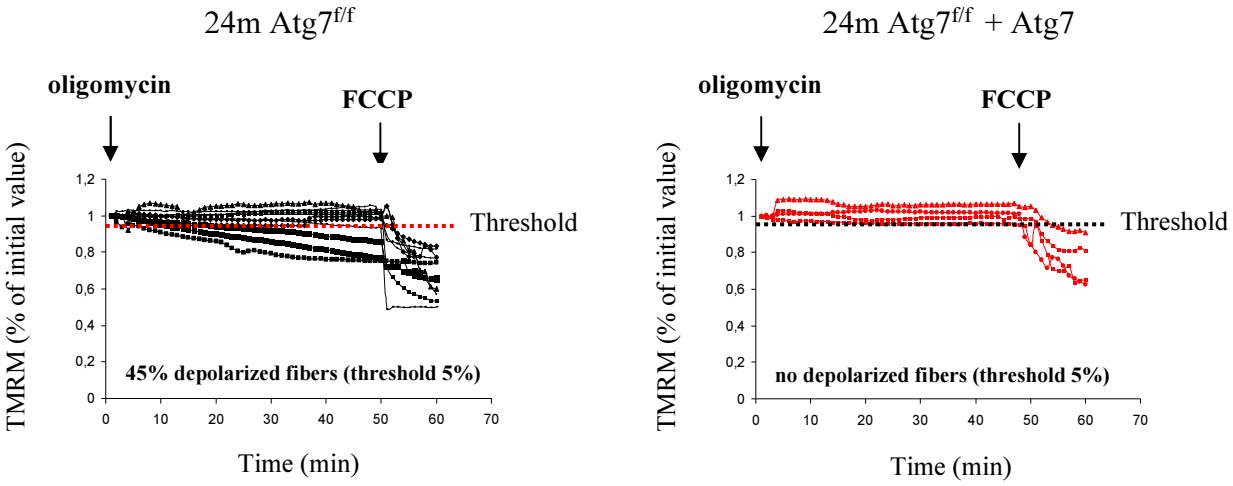

B

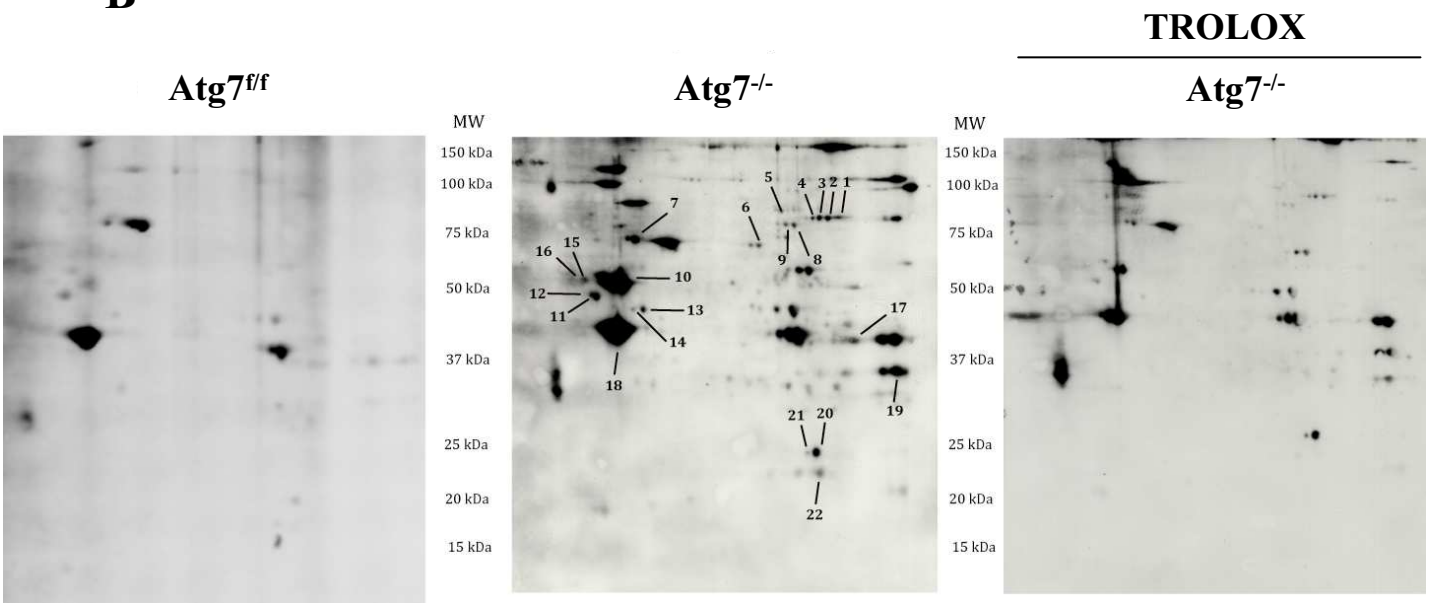

C

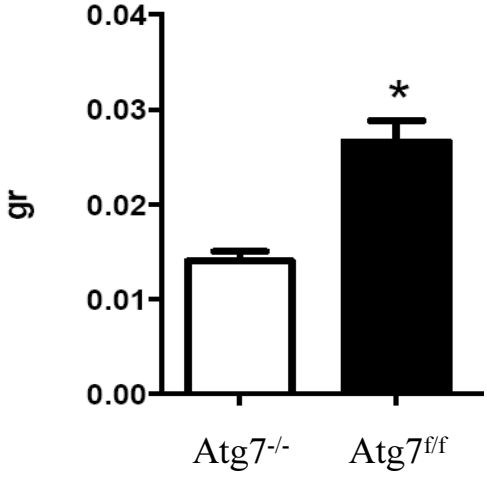

Atg7$^{-/-}$

Mean	SD	N
0.014040	0.004623	21

Atg7$^{f/f}$

Mean	SD	N
0.026606	0.008957	16

Figure S5

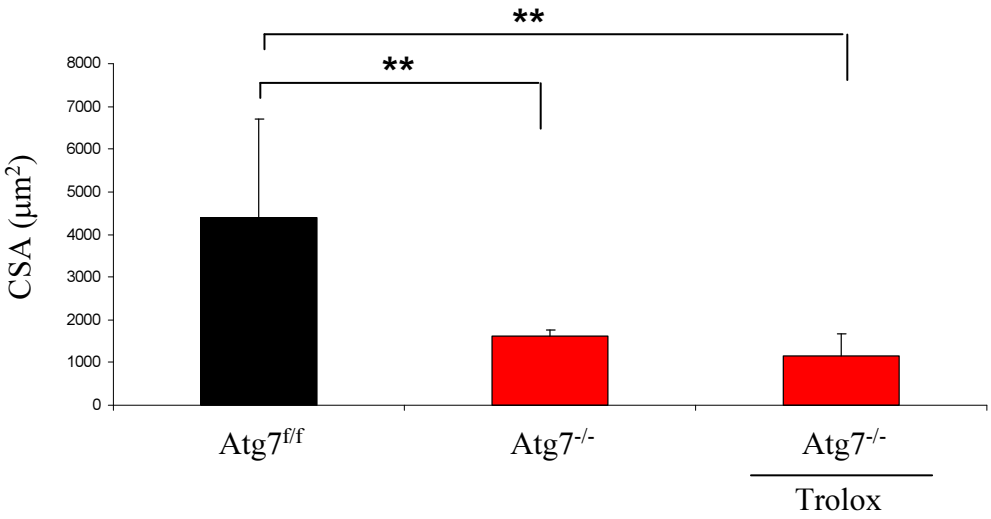
**
**
8000
7000
6000
5000
4000
3000
2000
1000
0
CSA (μm2)
Atg7f/f
Atg7-/-
Atg7-/-
Trolox

Figure S1. Morphological and functional impairment in muscles of *Atg7*$^{-/-}$ mice, related to Figure 2.

A. H&E staining of aged *Atg7*$^{f/f}$ and *Atg7*$^{-/-}$ Tibialis Anterior (TA) muscles shows that *Atg7*$^{-/-}$ muscles are atrophic with interstitial inflammation and center-nucleated fibers.

B. Representative images of immunostaining for Neural Cell Adhesion Molecule (NCAM) expression in aged *Atg7*$^{f/f}$ and *Atg7*$^{-/-}$ mice. Localization of NCAM along the entire fibers underlines the loss of muscle-nerve interaction.

Figure S2. Changes in NMJ are not secondary to p62 accumulation into aggregates, related to Figure 3.

A. Representative images of immunostaining for p62, that was knocked down *in vivo* in *Atg7*$^{-/-}$ mice, to reduce its content and the aggregates.

B. Quantification of NCAM positive fibers. Despite the absence of p62-positive aggregates, the percentage of denervated NCAM-positive fibers was not ameliorated.

Figure S3. Distribution of Cross Sectional Area in aged inducible *Atg7*$^{-/-}$, related to Figure 4.

Fiber size distribution analysis after acute *Atg7* deletion in aged mice revealed an enrichment in small fibers when compared to controls.

Figure S4. Autophagy is critical for mitochondrial function, oxidative stress and force generation, related to Figure 6.

A. TMRM analysis of mitochondria from aged *Atg7*$^{-/-}$ mice transfected with (right) or without (left) *Atg7* gene. Rescue of *Atg7* rescued the ability of aged mitochondria to maintain their membrane potential.

B. Proteomic analyses of carbonylated substrates. On the left proteins from *Atg7*$^{f/f}$ muscles; in the center proteins from *Atg7*$^{-/-}$ muscles; on the right: proteins from *Atg7*$^{-/-}$ muscles after treatment with anti-oxidant Trolox.

C. Muscle fibers from *Atg7*$^{-/-}$ muscles display less force than age-matched controls.

Figure S5. Trolox treatment did not rescue the atrophy of *Atg7*$^{-/-}$ mice, related to Figure 7.

Atrophy of *Atg7*$^{-/-}$ mice was not ameliorated upon anti-oxidant treatment.

Table S1

Protein spot no[a]	Protein	Swiss-Prot accession	Mascot score [c]	Sequence coverage (%)[d]	Matched Peptides[e]	Theoretical protein mass (Da)[g]	Theoretical PI[h]	RMI ratio[i] Atg$^{-/-}$/ Atg$^{f/f}$	RMI ratio Atg$^{-/-}$ Trolox / Atg$^{-/-}$
1	Aconitate hydratase	Q99KI0	283	30	7/18	85,464	8,1	1,56	0,28
2	Aconitate hydratase	Q99KI0	736	47	10/20	85,464	8,1	1,59	0,58
3	Aconitate hydratase	Q99KI0	192	17	5/10	85,464	8,1	1,42	>0,8
4	Aconitate hydratase	Q99KI0	168	9	5/7	85,464	8,1	1,56	>0,8
5	Glycogen phosphorylase, muscle form	Q9WUB3	172	23	5/17	97,286	6,7	3,76	0,55
6	Succinate dehydrogenase	Q8K2B3	395	47	10/20	72,585	7.06	1,65	0,35
7	Heat shock cognate 71 kDa protein	P63017	273	28	10/12	70,871	5,4	1,25	0,42
8	Pyruvate kinase isozymes M1/M2	P52480	688	50	8/20	57,845	7,2	2,44	0,66
9	Pyruvate kinase isozymes M1/M2	P52480	548	42	8/18	57,845	7,2	1,72	0,71
10	Desmin	P31001	487	48	11/18	53,498	5,2	3,78	0,23
10	Vimentin	P20152	57	4	2/2	53,688	5,1	3,78	0,23
11	Tubulin alpha-4A chain	P68368	117	27	6/8	49,924	5,0	3,16	0,47
12	Tubulin alpha-4A chain	P68368	61	6	2/2	49,924	5,0	1,30	0,44
13	Cytochrome b-c1 complex subunit 1	Q9CZ13	168	34	9/12	52,769	5,8	1,30	0,30
14	Cytochrome b-c1 complex subunit 1	Q9CZ13	87	24	2/10	52,769	5,8	2,72	0,57
15	ATP synthase subunit beta	P56480	902	59	12/20	56,300	5,2	2,44	0,51
16	ATP synthase subunit beta	P56480	732	50	12/18	56,300	5,2	1,39	0,46
17	Fructose-bisphosphate aldolase A	P05064	77	60	11/14	39,356	8,3	2,59	0,41
18	Actin, alpha skeletal muscle	P68134	810	47	7/12	42,051	5,2	1,35	0,67
19	Glyceraldehyde-3-phosphate dehydrogenase	P16858	812	42	7/8	35,810	8,4	1,3	0,32
20	Triosephosphate isomerase	P17751	1113	65	13/13	26,713	6,9	2,9	0,56
21	Triosephosphate isomerase	P17751	1148	65	13/13	26,713	6,9	1,4	0,48
22	Myoglobin	P04247	723	68	8/8	17,070	7,1	1,9	0,28

Table S1. Spots of interest identified by MS described in Experimental procedures and shown in Figure S4-B ,related to Figure 6 and Figure S4-B. Protein spots no (a) refer to numbered spots on Fig S6. For each spot, different parameters clarifying protein identification by MS are indicated [accession number (b), mascot score (c), % sequence coverage (d), no. of matched peptides (e), no. of sequenced peptides (f), theoretical protein mass (g) and theoretical PI (h)]. RMI ratio (i) represents the Relative Modification Index Ratio.

SUPPLEMENTAL EXPERIMENTAL PROCEDURES

Oligo sequence (5'-3').

shRNA oligos	Oligo sequence (5'-3')
p62/SQSTM1	Fw: TGCTGAGAGACTGGAGTTCACCTGTAGTTTTGGCCACTGACTGACTACAGGTGCTCCAGTCTCT Rev: CCTGAGAGACTGGAGCACCTGTAGTCAGTCAGTGGCCAAAACTACAGGTGAACTCCAGTCTCTC

Primers for quantitative Real Time PCR (qRT-PCR) analyses.

qRT-PCR primer	Oligo Sequence (5'-3')
m-AChRγ	Fw: CAGTGGGGGACCTAGAAACA Rev: ACCTTTCCAATCCACAGCAC
m-MuSK	Fw: ATCACCACGCCTCTTGAAAC Rev: TGTCTTCCACGCTCAGAATG
m-PAN-ACTIN	Fw: CTGGCTCCTAGCACCATGAAGAT Rev: GGTGGACAGTGAGGCCAGGAT
m-h-GAPDH	Fw: TGCACCACCAACTGCTTAGC Rev: GGCATGGACTGTGGTCATG

Antibodies

Primary Antibodies	**Company**
anti-ATG7	Sigma
anti-LC3	Sigma
anti-GAPDH	Abcam
anti-NCAM	Millipore
anti-P62	Sigma
anti-pan actin	Sigma
Secondary Antibodies	
anti-mouse Alexa Fluor 488 and 594	Life Technologies
anti-rabbit Alexa Fluor 488 and 594	Life Technologies
anti-mouse HRP Conjugate	Bio-rad
anti-rabbit HRP Conjugate	Bio-rad

Protein Carbonyls Detection and anti-oxidant treatment

For proteomic analyses, gastrocnemius muscle derived wild-type, Atg7 KO mice and Atg7 KO mice treated with Trolox (three animals per group), were homogenized in an UltratoraxTM homogenizer (low setting, 3 s) using a lysis buffer (10 mM tris-HCl (pH 7.4), 8 M urea, 2 M thiourea, 4% (w/v) CHAPS) and clarified by centrifugation. Proteins in the supernatant were precipitated using the 2-D Clean-Up kit (GE Healthcare) following the manufacturer instructions. Protein precipitates were then resuspended in lysis buffer and protein quantification was performed using the Bradford method (Pierce), using bovine serum albumin as a standard. Protein carbonyl detection was performed using OxyBlotTM, according to manufacturer instructions. For 1D Oxyblot, 15 µg of protein lysates were derivatized with 2,4dinitrophenylhydrazine followed by SDS-PAGE (12% (v/v) polyacrylamide) separation and electro blotting onto nitrocellulose membranes. After blocking, membranes were incubated with anti-DNP antibodies, washed, and incubated with peroxidase conjugated anti-rabbit IgG antibodies. 2D Oxyblot was performed in protein extracts derived from the same samples used for 1D Oxyblot, after 2D PAGE separation as described previously (Baraibar et al., 2011). For each sample two gels were performed in parallel, one for colloidal blue staining of total proteins and other for electroblotting onto nitrocellulose membranes. Membranes were then incubated for 2 h in the blocking solution and carbonyl detection was performed using the OxyBlotTM kit, as described above. Membranes were developed using Amersham ECL Plus Western Blotting Detection System. Films were digitized with UMAX UTA-100 scanner (GE Healthcare) and densitometry analyses were performed using NIH ImageJ or Image Master 2D Platinum 7 software (GE Healthcare).

2D-OxyBlot data acquisition and analysis.

For each spot identified by coomassie blue as well as from the OxyBlot a percentage volume was obtained in pixels (%Vol). The %Vol corresponds to a normalized value of the spot volume by considering the total volume of all the spots present in the gels or on films. %Vol of carbonylated spots from $Atg7^{f/f}$, $Atg7^{-/-}$, and $Atg7^{-/-}$ Trolox were normalized with %Vol of the corresponding Coomassie-stained spot to obtain a normalized %Vol (N%Vol). The N%Vol of spots derived from $Atg^{-/-}$ were divided by the N%Vol of $Atg7^{f/f}$ to obtain the Relative Modification Index ratio (RMI ratio). In addition the ratio $Atg7^{-/-}$ Trolox / $Atg7^{-/-}$ was performed after Trolox tratment. Spots with an RMI ratio ≥1.2 are considered as oxidatively modified in $Atg7^{-/-}$ and spots with a RMI ratio <0,8 are considered as decreased after Trolox treatment.

In-gel digestion, mass spectrometry protein identification and database searches.

Spots of interest were manually excised from gels and proteins were digested with trypsin. Peptide mass spectra were acquired in positive reflector mode on a 4800 Plus MALDI TOF/TOF™ Analyzer (Applied Biosystems, Foster City, CA, USA) using 20 kV of acceleration voltage. Each spectrum was externally calibrated using peptides derived by tryptic digestion of ß-lactoglobulin. Tandem mass spectra were acquired using the same instrument in MS/MS positive mode. Output peak lists were generated using Data Explorer (Applied Biosystems, Foster City, CA, USA) from the raw data. MS and MS/MS peak lists were combined into search files and used to search SwissProt database using the Mascot search engine (Matrix Science Ltd, London, UK). Search parameters were as follows: Database: SwissProt; Taxonomy: all entries or mammalian; Enzyme: trypsin; Allow up to 1 missed cleavage; Fixed modifications: none; Variable modifications: methionine oxidation; Peptide mass tolerance: 70 ppm; and Fragment mass tolerance: 500 ppm. Mascot protein scores greater than 56 are significant at $p<0.05$.